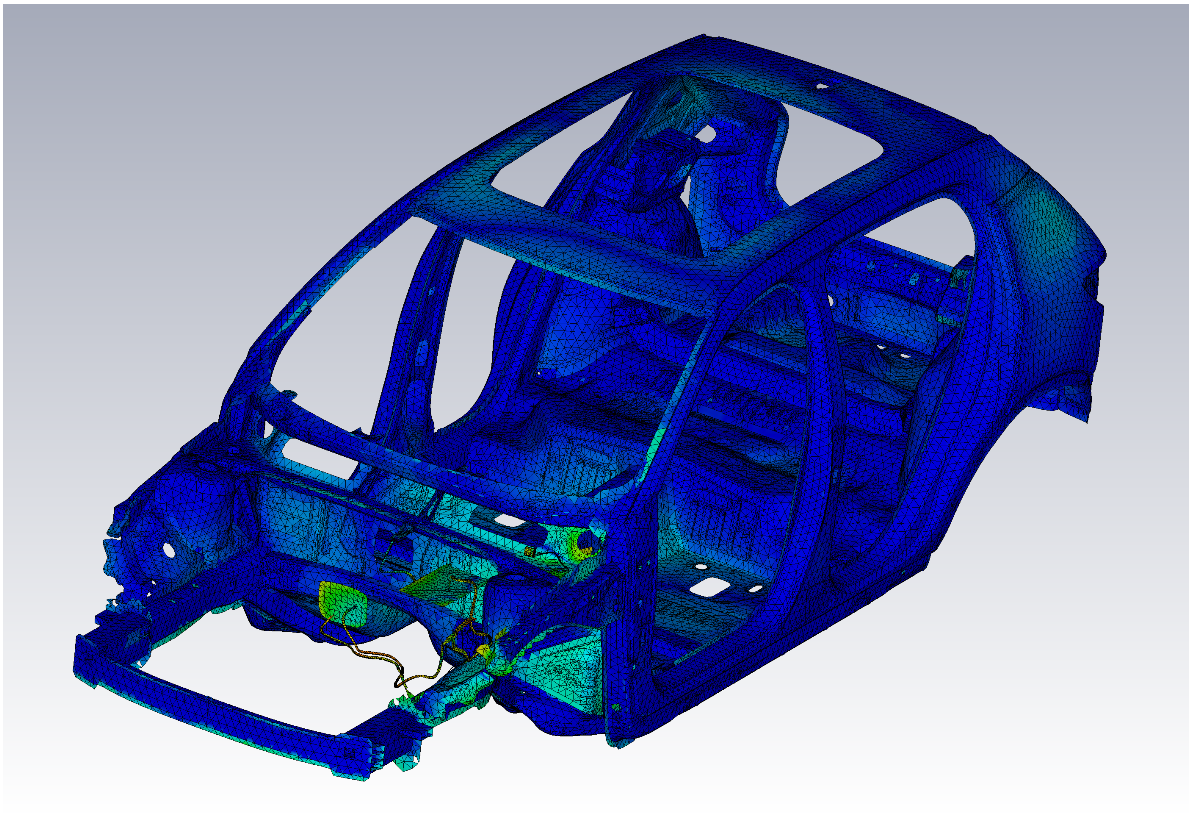

Vehicle Level EMC Performance Prediction from Component Test Results

Master’s thesis in Sustainable Electric Power Engineering and Electromobility

WENDA LI & SHINUO FANG

DEPARTMENT OF ELECTRICAL ENGINEERING

CHALMERS UNIVERSITY OF TECHNOLOGY
Gothenburg, Sweden 2025
www.chalmers.se

Master's thesis 2025

Vehicle Level EMC Performance Prediction from Component Test Results

WENDA LI & SHINUO FANG

Division of Electric Power Engineering
Department of Electrical Engineering
Chalmers University of Technology
Gothenburg, Sweden 2025

Vehicle Level EMC Performance Prediction from Component Test Results
WENDA LI & SHINUO FANG

Supervisor: Helin Zhou, VOLVO CARS
Examiner: Yujing Liu, Department of Electrical Engineering

Master's Thesis 2025
Division of Eletric Power Engineering
Department of Electrical Engineering
Chalmers University of Technology
SE-412 96 Gothenburg
Telephone +46 31 772 1000

Typeset in LaTeX
Printed by Chalmers Reproservice
Gothenburg, Sweden 2025

Vehicle Level EMC Performance Prediction from Component Test Results
WENDA LI & SHINUO FANG
Department of Electrical Engineering
Chalmers University of Technology

Abstract

This thesis investigates the feasibility of predicting vehicle-level Electromagnetic Compatibility (EMC) performance from component-level testing and simulation. Using an automotive wiper drive system as the case study, the work aims to reduce dependence on costly and time-consuming whole-vehicle EMC tests by establishing an integrated methodology combining empirical measurement and numerical modeling. Component-level conducted and radiated emission tests were performed in accordance with Comité International Spécial des Perturbations Radioélectriques (CISPR) 25, and the measured common-mode currents were used as excitation sources in Computer Simulation Technology (CST) Studio Suite simulations. The correlation between measured and simulated electric fields in the 150 kHz–30 MHz range showed close agreement, confirming that measurement-driven source modeling can accurately reproduce radiated emission behavior. The validated component model was then extended to a full-vehicle electromagnetic simulation, where near-field coupling and grounding effects were analyzed. Results indicate that component-based models can qualitatively predict vehicle-level trends, offering engineers an early-stage diagnostic tool for identifying potential EMC risks. Although full substitution of physical vehicle testing remains challenging due to modeling and computational limitations, the proposed hybrid workflow demonstrates a practical pathway toward simulation-supported EMC development, aligning with the automotive industry's goals for faster, more efficient, and cost-effective design validation.

Keywords: Electromagnetic Compatibility (EMC), Electric Vehicles (EV), Numerical Modelling, Simulation, Component-level Testing, CAE Modelling, CST.

Acknowledgements

We would first like to express our sincere gratitude to our supervisor Dr. Helin Zhou from Volvo Cars. He has provided patient and detailed guidance on the project scope, the technical approach, the measurement setups, the simulation configuration and the interpretation of the results, as well as on the overall structure of the thesis. His continuous and insightful feedback has been essential for the direction and completeness of this work.

We are also grateful to Professor Yujing Liu from the Department of Electrical Engineering at Chalmers University of Technology, the examiner of this thesis, for his academic guidance and valuable comments. His expertise in electromagnetic compatibility has helped us to clarify our research focus and to improve both the structure and the clarity of the thesis.

We thank Dimitrios Sagris from Volvo Cars to provide the measurement support during EMC component-level test in the semi-anechoic chamber. We also would like to thank Håkan Ringius and Krzysztof Siedlecki to prepare the car body and wire harness models for EMC simulations.

Finally, we would like to thank our manager Dr. Mattias Ingvarson from Volvo Cars for his support and trust in this project. He provided the necessary resources and a good working environment, which enabled us to carry out the measurements and simulations in a realistic industrial context.

Wenda Li & Shinuo Fang, Gothenburg, December 2025

Statement on the Use of AI Tools

In accordance with Chalmers regulations on the use of AI tools in theses, this work acknowledges limited and transparent use of AI-based assistance.
AI tools (OpenAI ChatGPT and Google Gemini) were used only for:

- improving language clarity and grammar in parts of the text;
- occasional translation assistance when drafting from another language.

AI tools were **not** used to generate technical content, data, analysis, figures, or research results. All methodology, experiments, data processing, and conclusions were carried out independently by the authors. The use of AI tools was strictly restricted to writing support and did not influence the technical substance of the thesis.

List of Acronyms

Below is the list of acronyms that have been used throughout this thesis listed in alphabetical order:

AF	Antenna Factor
AI	Artificial Intelligence
AVG	Average
BIW	Body-in-white
BiCD	Bipolar-CMOS-DMOS
CAE	Computer-Aided Engineering
CAN	Controller Area Network
CE-derived	Conducted Emission-derived
CEM	Central Electronic Module
CISPR	Comité International Spécial des Perturbations Radioélectriques
CM	Common-mode
DPI	Direct Power Injection
ECE	Economic Commission for Europe
ECPM	Extended Chip Power Model
ECU	Electronic Control Unit
EM	Electromagnetic
EMC	Electromagnetic Compatibility
EMP	Electromagnetic Pulse
EMT	Electromagnetic Topology
EV	Electric Vehicles
FDTD	Finite-Difference Time-Domain
FEM	Finite Element Method
FPC	Flexible Printed Cable
GB	Guobiao (Chinese National Standards)
HF	High Frequency
HVAC	Heating, Ventilation and Air Conditioning
IEC	International Electrotechnical Commission
IGBT	Insulated Gate Bipolar Transistor
ISO	International Organization for Standardization
KPI	Key Performance Indicator
LF	Low Frequency
LIN	Local Interconnect Network
LISN	Line Impedance Stabilization Network

LPDA	Log-Periodic Dipole Antenna
MoM	Method of Moments
OEM	Original Equipment Manufacturer
PCB	Printed Circuit Board
PEC	Perfect Electric Conductor
PHY	Physical Layer
PK	Peak
RFI	Radio Frequency Interference
RF	Radio Frequency
RGB	Red, Green, Blue
RMS	Root Mean Square
RMSE	Root Mean Square Error
SAC	Semi-Anechoic Chamber
SAE	Society of Automotive Engineers
TFT-LCD	Thin-Film Transistor Liquid Crystal Display
UHF	Ultra High Frequency
V2X	Vehicle-to-Everything
VHF	Very High Frequency
VSWR	Voltage Standing Wave Ratio

Contents

List of Figures

List of Tables

1

Introduction

1.1 Background

In contemporary society, the automotive industry is experiencing a profound transformation, driven by a combination of policy and regulatory forces, rapid technological advancements, and sustained market demands. This transformation is characterized by the integration of advanced electronic systems and the adoption of electrification technologies. This transformation reshaped the development process of modern vehicles and places increasing emphasis on electromagnetic compatibility (EMC) fundamentally. Ensuring EMC has become a critical requirement due to the introduction of complex electromagnetic environments and new sources of interference from high-voltage powertrains, digital control modules, and connected communication technologies[1]. Conventional EMC verification is primarily executed through late-stage vehicle-level testing. While such testing ensures compliance, it is expensive, time-consuming, and may require significant design modifications if defects are identified at a late stage. Current international standards, including the International Special Committee on Radio Interference (CISPR)[2], the International Organization for Standardization (ISO)[2], and the Chinese National Standards (Guobiao, GB)[3], provide harmonized procedures for emissions and immunity testing. However, these standards are often insufficiently adaptable to new technologies and cannot fully capture realistic operating conditions. Furthermore, it should be noted that compliance at the component level does not necessarily guarantee compliance at the vehicle level. This is due to the fact that interactions with vehicle body structures, wiring harnesses, and grounding schemes may significantly electromagnetic behavior[4]. These challenges underscore the necessity for predictive methodologies that facilitate early-stage EMC evaluation.

1.2 Aim

The objective of this thesis is to explore the potential of utilizing component-level EMC test results to enhance the prediction of vehicle-level EMC performance. The wiper drive system is selected as a case study due to its relevance as a common source of radiated and conducted emissions. The primary aim of this research is to develop and refine a numerical modeling methodology that strengthens the correlation between component- and vehicle-level performance. The present study proposes a framework for early-stage EMC prediction, with the objective of reducing reliance on late-stage full-vehicle testing, enhancing design efficiency, and supporting compliance with CISPR 25 standards. This framework integrates experimental testing with electromagnetic simulation.

1.3 Scope

The scope of this research includes both experimental and modeling activities. At the component level, EMC testing of the wiper motor and controller will be conducted in a semi-anechoic chamber (SAC) to characterize conducted and radiated emissions. The resulting data will serve as the basis for developing numerical models in Computer Simulation Technology (CST) Studio Suite, which will be refined through iterative adjustments of material properties, boundary conditions, and excitation methods. Later a comparative analysis will be performed between simulation and measurement results to evaluate the predictive reliability of the model. At the system level, the employment of simulation models will facilitate the consideration of vehicle-specific factors, including body shielding, wiring harness coupling, and grounding effects.

2

Theory

2.1 Fundamentals of EMC

Electromagnetic compatibility (EMC) is defined as the capability of an electrical or electronic system to function satisfactorily within its intended electromagnetic environment without generating intolerable electromagnetic disturbances to other equipment[1]. This definition underscores the dual nature of EMC: on the one hand, a system must not emit excessive electromagnetic energy that interferes with other devices; on the other hand, it must maintain stable performance when exposed to external interference[5].

In the automotive industry, EMC issues are particularly evident due to the integration of high-voltage and low-voltage systems within a confined space. The most common sources of interference include electric drive systems(inverters and electric machines), DC–DC converters, as well as in-vehicle devices such as windshield wipers and window actuators. Coupling paths exist in two domains: the conducted domain and the radiated domain. The conducted domain includes wiring harnesses and common grounding, while the radiated domain includes antenna-like structures formed by cables and metallic body panels[6]. Systems that are particularly vulnerable to interference frequently encompass safety-related subsystems, such as the electronic control unit (ECU), sensor networks, in-vehicle entertainment modules, and wireless communication interfaces. This can be depicted in Fig. 2.1.

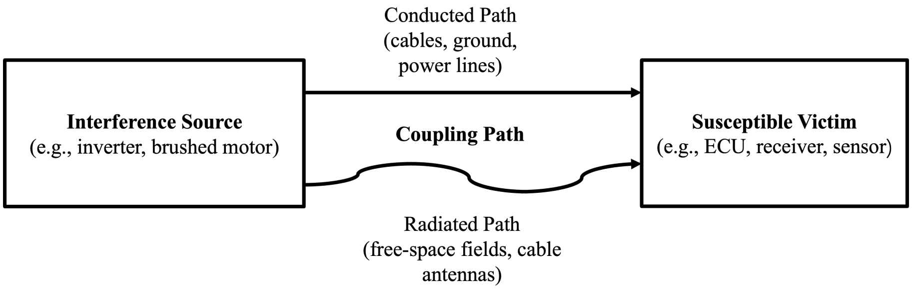

Figure 2.1: Relationship Between Interference Source, Coupling Paths, and Susceptible Victim.

2.2 Automotive EMC Testing and Standards

Current international automotive EMC standards are mainly composed of four systems: CISPR, ISO, the Society of Automotive Engineers (SAE), and GB. CISPR, under the International Electrotechnical Commission (IEC), focuses on radio-frequency interference (RFI) limits and measurement methods, particularly emission control. ISO Technical Committee 22/Subcommittee 3/Working Group 3 (ISO/TC 22/SC 3/WG 3) specifies electromagnetic immunity test methods for vehicles[7], with the ISO 11451 and ISO 11452 series widely adopted for whole-vehicle and component-level immunity evaluations. CISPR 12 and CISPR 25 regulate emission limits for complete vehicles and components to protect both the external radio environment and on-board receivers. SAE standards, though mainly applied in North America, have gradually been replaced or integrated with equivalent CISPR and ISO standards as global harmonization progresses[8]. Meanwhile, GB standards in China align closely with CISPR and ISO frameworks while incorporating domestic regulatory requirements, ensuring compatibility with international practices but also addressing local compliance needs[3].

Together, these standards form the foundation of global automotive EMC assessment. Many national regulations, such as the United Nations Economic Commission for Europe Regulation No. 10 (ECE R10), also CISPR and ISO[9], reinforcing harmonization across regions. However, despite their wide application, these standards remain limited in adapting to emerging technologies and do not always reflect realistic operational conditions. Moreover, compliance at the component level does not necessarily ensure compliance at the vehicle level, as interactions with body structures, wiring harnesses, and grounding schemes may alter electromagnetic performance[4].

Regarding test implementation, there are notable differences between vehicle-level and component-level methods. For radiated emissions, vehicle-level testing (CISPR 12) typically measures broadband disturbances in the 30–1000 MHz range at a specified distance in an open field environment[7]. In contrast, component-level testing (CISPR 25) is carried out in a shielded dark room over a wider frequency range[10], and focuses on evaluating interference to on-board receiving equipment[7]. CISPR 25 also defines a vehicle self-compatibility test, which measures noise using the vehicle antenna and links the EMC performance of components to that of the complete vehicle through multiple levels of limits.

In terms of immunity, the ISO 11452 series specifies various component-level test methods[11][12], each with its own frequency range and size constraints, while ISO 11451 provides vehicle-level immunity test procedures that more closely represent the real operating environment. Component-level compliance establishes the foundation for vehicle-level performance, whereas vehicle-level testing validates the overall effect of actual installation. In practice, both levels of testing are indispensable.

However, the current EMC test system still has limitations in practical applications. Firstly, the standards are not sufficiently adaptable. Automotive electronics evolve rapidly, while standard updates lag behind[13], and many test assumptions are too idealized to fully reflect real operating conditions. For example, the transient pulse defined by ISO 7637-2 is considered too simplistic: although no abnormalities are observed under the standard pulse, real transient interference in the vehicle may still cause the ECU to malfunction. Conversely, problems measured in the laboratory may not be reproduced in the actual vehicle[14]. Secondly, it is difficult to derive vehicle-level performance directly from component-level test results. Passing component-level tests does not necessarily imply full-vehicle compliance with EMC requirements. In some cases, the shielding provided by the vehicle structure may make independent component requirements overly conservative, while the coupling of components within the vehicle may generate unexpected interference not observed at the bench level. Therefore, vehicle-level testing remains necessary to confirm compliance; however, this leads to duplicated processes and extended development cycles. Moreover, vehicle testing is costly, and expenses and schedule pressure increase significantly if retesting is required in the later stages.

Facing the trends of electrification and intelligentization, the adaptability of existing standards is increasingly challenged. High-voltage electric drives and intelligent connected technologies are reshaping the electromagnetic environment of vehicles and expanding the noise spectrum beyond the range covered by current standards. The slow pace of standard updates compared with technological development means that traditional methods can no longer fully ensure the electromagnetic robustness of future vehicles[13]. As a result, simulation technology has emerged as an essential development direction. Numerical analysis can be used to analyze field distributions and compensate for blind spots in physical measurements, while simulation methods such as cable harness current prediction can assist in evaluating EMC performance during the design stage[15]. These approaches are expected to improve testing efficiency and accelerate the evolution of standards to address the challenges posed by electrification and intelligence.

2.3 Automotive EMC Simulation Technology

The increasing complexity and electrification of automotive electronic systems have brought electromagnetic compatibility (EMC) issues into greater prominence[16]. Traditional EMC tests are usually conducted at the late stage of product development, often during vehicle prototyping, when any problems discovered may lead to costly modifications and significant delays in product schedules[17]. To improve development efficiency, manufacturers and researchers are increasingly introducing simulation into the early design phase to predict and analyze potential EMC problems[16][18]. Simulation enables engineers to evaluate the impact of design choices—such as adjusting wiring layouts, adding shielding, or implementing filters—within a virtual environment, thereby reducing the number of costly iterations in prototyping and physical testing[19].

Current automotive EMC simulation approaches include circuit simulation, 3D full-wave electromagnetic simulation, and circuit–electromagnetic joint simulation. Full-wave electromagnetic simulation is based on solving Maxwell's equations and can accurately model the radiation of high-frequency electronic components using algorithms such as the Finite Difference Time Domain (FDTD) method, the Finite Element Method (FEM), and the Method of Moments (MoM). For instance, Wang et al. used 3D full-wave modeling to analyze the radiation disturbances of a digital instrument display module and proposed an optimized signal integrity design that effectively reduced electromagnetic emissions[20]. Jobava et al. developed an efficient integral equation algorithm for low-frequency magnetic field analysis, which significantly improved the efficiency of analyzing high-voltage cables and inductive charging devices in electric vehicles[21]. Meanwhile, high-performance computing (HPC) techniques have also been introduced into EMC simulation; for example, Hänninen et al. applied domain decomposition, GPU acceleration, and model segmentation to improve the efficiency of 3D full-wave simulation, making it possible to include complex printed circuit boards (PCBs) and long wiring harnesses in the simulation[18].

Circuit–electromagnetic joint simulation, which considers the coupling between nonlinear circuits and electromagnetic fields, is particularly suitable for power electronic systems such as automotive motor drives and high-voltage inverters. In the Electromagnetic Interference(EMI) analysis of high-voltage inverters, for instance, it is necessary to simulate both the interference caused by high di/dt switching currents of insulated gate bipolar transistors (IGBTs) and the radiative coupling of these currents through wiring and structures[22]. Murugan et al. successfully predicted the conducted and radiated emissions of an automotive DC-DC converter through multi-scale modeling, with results that closely matched laboratory measurements[23]. Ahmed et al. employed a hybrid solution approach that combined frequency-domain full-wave electromagnetic simulation with circuit simulation to model electromagnetic pulse (EMP) interference[24]. This method significantly reduced computation time while still achieving high accuracy in calculating induced voltages and currents on sensitive components.

More recently, multi-port network modeling has been introduced for system-level EMC analysis. Wu et al. established a whole-vehicle electromagnetic disturbance prediction model based on the electromagnetic topology (EMT) method[16]. By dividing the complex system into multiple subsystems and modeling them separately, they were able to quickly evaluate the radiation disturbance level of the entire vehicle through extracted network parameters. This method demonstrated strong consistency with experimental measurements in low-frequency radiation prediction, proving its effectiveness for rapid system-level analysis. Gao et al. further applied this approach to optimize the low-frequency radiated emission problem of an electric vehicle. They modeled the whole vehicle as several interconnected modules and, after extracting parameters through testing and simulation, found that the predicted interference peaks differed from the actual measurements by less than 3 dB[17]. Multi-port modeling is particularly well-suited for topologically complex systems such as wiring harnesses, and when combined with circuit simulation, it provides an efficient tool for rapid and accurate system-level EMC evaluation.

2.4 EMC Simulation Case Study

The following is an example of several typical vehicle electronic systems to summarize the effect and experience of EMC simulation technology in practical applications.

2.4.1 EMC Simulation of Motor Drive System

The three-phase drive motor and its inverter in an electric vehicle are among the main sources of EMI, as the fast switching of high voltage and high current produces disturbances across a wide frequency band. Ming et al. (2024) conducted an EMC simulation study for the electric drive system of an electric construction machine[25]. They established an equivalent circuit model that included the power battery, the inverter (comprising IGBT power devices and control circuits), the motor, and the test harness, and focused on simulating and analyzing the conducted interference on the DC bus of the inverter. A low-pass filter consisting of an inductor and a capacitor was introduced into the simulation. The results showed that, compared to the case without a filter, the amplitude of the conducted disturbances in the drive system was significantly reduced. In addition, the DC bus current ripple and the high-frequency noise of the output voltage were effectively suppressed, and the low-frequency offset of the signal was also improved[25]. This study demonstrates that through reasonable equivalent model construction and circuit simulation, the effectiveness of EMC improvement measures such as filters can be verified already at the design stage, thereby reducing the costs associated with repeated prototype debugging.

2.4.2 EMC simulation of digital display module

With the shift from mechanical pointers to fully digital displays for in-vehicle instrumentation and central control, the high-speed digital interfaces of display modules have become one of the key challenges in EMC design. Wang et al.(2018) conducted an EMC performance study of an automotive digital instrument cluster display module using 3D full-wave electromagnetic simulation (i.e, CST)[20]. Their findings showed that in the original design, the pixel clock line (30 MHz clock driving parallel Red, Green, and Blue (RGB) data) of the Thin-Film Transistor Liquid Crystal Display (TFT-LCD) display lacked a proper return path on the flexible printed cable (FPC). As a result, high-frequency currents were forced to bypass, forming a large loop that generated significant electromagnetic radiation[20].

Through simulation, the current distribution of the clock line at 90 MHz resonance was visualized, revealing the underlying problem. Based on this analysis, several improvement schemes were proposed: adding ground returns to the adjacent layers of the clock line in the FPC, introducing ground vias, and optimizing the integrity of the power–ground planes. The optimized layout was then simulated, confirming that the high-frequency current loop was significantly reduced and the far-field radiation in the 100–400 MHz band was greatly suppressed[20].

Ultimately, the researchers were able to evaluate multiple design options rapidly through virtual prototyping and apply targeted modifications to the PCB routing of the display module, thereby addressing potential EMC hazards without increasing the number of hardware trials. This case demonstrates that full-wave simulation, combined with signal and power integrity analysis, can effectively guide the EMC design of high-speed digital systems, offering a cost-efficient approach to the optimization of complex modules such as thin automotive displays.

2.4.3 EMC Simulation of Automotive Ethernet Interface

Automotive Ethernet is increasingly becoming the backbone of in-vehicle communication due to its high speed and reliability. However, if the differential signals of the Ethernet Physical Layer (PHY) interface are not properly routed, they can generate common-mode noise that radiates and interferes with other electronic devices. Andrei-Marius Silaghi et al. (2020) conducted an EMC simulation analysis of an in-vehicle Ethernet control module[26]. Using CST, they performed 3D electromagnetic modeling of the differential pairs in the PHY chip and their associated PCB traces, calculated the S-parameters of the differential ports, and evaluated key indicators such as mode conversion loss (differential to common mode) and return loss.

The simulation revealed that in the original PCB design, the mode conversion loss exceeded the threshold defined by the Open Alliance Automotive Ethernet standard in the frequency range above 300 MHz, indicating that design improvements were necessary[26]. To address this, the researchers proposed two optimization measures: (1) partitioning and isolating the PCB ground according to functional blocks to reduce coupling between different modules; and (2) optimizing the routing of high-speed differential lines to ensure they consistently return to symmetric reference planes above and below. After implementing these measures, the improved structure was simulated again, and both the mode conversion loss and return loss curves met the standard requirements[26]. Notably, at the frequencies where the original design exceeded the limit, common-mode noise radiation decreased significantly, confirming the effectiveness of the split-grounding and differential-line equalization strategies. This case illustrates how simulation can help identify potential EMC problems of high-speed digital interfaces at an early stage and guide PCB design modifications, thereby avoiding repeated trial-and-error in later hardware experiments.

2.4.4 EMC Simulation of Integrated Circuit Modules

For critical integrated circuit (IC) devices in automotive electronics, internal parasitic coupling and package lead distribution can directly influence the EMC performance of the entire module. Tsukioka et al. (2017) proposed a joint chip–package–system EMC simulation methodology for automotive ICs[27]. In this approach, they introduced the concept of the Extended Chip Power Model (ECPM), which represents the power network, substrate coupling, and isolation structures inside the chip as a passive multiport network in the form of a netlist. This netlist is then connected to the package and PCB models for comprehensive analysis.

To validate the methodology, the authors simulated and tested the direct power injection (DPI) immunity of a Local Interconnect Network (LIN) bus transceiver chip implemented in a 0.13 μm Bipolar-CMOS-DMOS (BiCD) process, following the IEC 62132-4 standard. The simulation successfully predicted the path of high-power RF interference entering the internal circuits through package leads and substrate coupling, and it identified the weak points in the LIN transceiver that were most susceptible to interference[27]. More importantly, the simulated responses of the chip's critical nodes showed strong consistency with silicon measurements, verifying both the accuracy of the ECPM model and the practical value of the joint simulation approach[27].

This research provides a new perspective on collaboration between chip suppliers and Original Equipment Manufacturers(OEMs) in the design of automotive electronics. By introducing EMC simulation at the IC design stage, potential radiation and susceptibility issues can be identified early, and EMC performance can be enhanced by optimizing the chip's internal layout and package structure. This reduces the burden of costly system-level rectifications for OEMs at later development stages.

2.5 Feasibility and Challenges of Component-Based EMC Simulation on the Vehicle-level

Utilizing the simulation results of local systems or components installed within the vehicle to replace vehicle-level EMC testing is a forward-looking topic in current automotive EMC engineering. The core idea is that through detailed modeling and calculation, the electromagnetic behavior of a component in its installed state can be reproduced in a virtual environment, so that the simulation results closely match those of real vehicle tests. The wiper motor provides a useful example for discussing both feasibility and challenges.

2.5.1 Feasibility Analysis

Wiper motors are typically brushed DC motors, whose commutators generate strong spark interference during operation, making them one of the major sources of RF disturbances in vehicles. Traditionally, OEMs and component suppliers perform bench tests of stand-alone wiper motors in the laboratory—for example, connecting the motor to a standard wiring harness length and placing it on a grounded reference plate to measure radiated and conducted noise in accordance with CISPR 25. This method simulates the motor's electromagnetic environment under standardized conditions. If a simulation model can reproduce the bench test conditions and results, it is further expected that the model could also be adapted to predict in-vehicle performance. The multi-port network approach of Gao et al. (2019) represents one such exploration: they modeled the vehicle's body and ground as large structures, while treating interference sources such as wiper motors as small components, and coupled them through network theory to calculate the whole-vehicle EMC[17]. In a scaled-down validation model (using reduced-size structures and antennas), the method successfully predicted the interference voltage spectrum received by the antenna with a deviation of less than 3 dB at the main resonance peak[17]. They later applied the method to an actual electric vehicle, accurately locating the major sources of interference and guiding corrective measures. This shows that component modeling combined with system-level network methods can, to some extent, predict the EMC performance of a whole vehicle, providing proof of concept for replacing part of the test with simulation.

2.5.2 Challenges

Difficulty in modeling interference sources. The EMI mechanisms inside components such as wiper motors are highly complex, especially the transient broadband interference from commutation sparks. Accurately characterizing these disturbance sources in simulation is a primary challenge. For example, Pan et al. (2015) attempted to extract the internal impedance and noise source voltage of motors using Thevenin equivalent circuit measurements[28], while Idir et al. (2009) developed a broadband equivalent model by combining time-domain and frequency-domain approaches[29]. These methods provide parameters for simulation but are often cumbersome and uncertain. If the source model lacks accuracy, the predictions will inevitably deviate from real measurements.

Complex vehicle environment. Even with a reliable source model, simulating the propagation of interference throughout an entire vehicle is difficult. Vehicle bodies include large metal structures, extensive glass areas, and numerous wiring harnesses, all of which create highly complex resonances and coupling paths[30]. For example, wiper motors are grounded via their supply harnesses, and variations in wiring routes or grounding points affect the radiated field strength received by antennas. Furthermore, many other metallic components and electronic devices may interact with or superimpose on the frequency components generated by the wiper motor. Fully modeling all vehicle details is currently computationally impractical, requiring simplifications. However, oversimplification risks omitting critical coupling paths and undermining credibility.

Simulation tools and calibration. For simulation results to be accepted by industry and regulators, a complete calibration framework is needed[15]. This involves selecting appropriate simulation tools and algorithms with controllable errors, validating accuracy through standardized experiments (such as harness radiation calibration or standard interference source verification), and defining unified evaluation metrics to quantify deviations between simulations and real measurements. While aerospace engineering has already begun discussing “simulation-based certification,” similar initiatives in the automotive sector are only just emerging. Thus, both technically and organizationally, replacing testing with simulation requires a gradual process of validation and acceptance.

In summary, using component-based simulation to predict whole-vehicle EMC performance holds great promise[31]. It can help engineers identify potential problems and optimize designs early in the virtual environment, reducing the number of physical tests and associated risks. However, fully replacing vehicle-level testing remains challenging and requires further research and accumulated experience. In the near term, simulation is better positioned as a complement rather than a substitute: narrowing down problem locations, assisting in design improvements, and ultimately verifying results with a limited number of vehicle tests. With continuous advances in simulation methods and computing power, this integrated approach will gradually shift automotive EMC development from a test-dominated process to one more reliant on simulation.

2.6 Future Trends in Automotive EMC Simulation

The research and application of automotive EMC simulation technology are continuously advancing. From the above overview, it is evident that with the growing complexity of electronic systems, simulation has become an indispensable tool for ensuring EMC performance. At present, whether at the level of local PCB traces, cable connectors, or vehicle-level antenna layouts and system coupling, there are corresponding simulation methods and case studies available. These technological developments enable engineers to identify EMC risks earlier and more proactively, addressing potential issues before bench testing. Numerous studies and practical applications have already demonstrated the value of simulation in reducing development costs and shortening debugging cycles.

2.6.1 Digital Twin and Real-time Simulation

With the development of Internet of Things(IoT) and big data technologies, the concept of the digital twin for vehicles will expand beyond powertrains and functional logic to also include EMC characteristics[32]. By integrating a high-fidelity EMC model into the digital twin and continuously updating it with real vehicle test data, manufacturers will be able to realize real-time monitoring and prediction of EMC performance. For example, when the configuration of a vehicle changes—such as the replacement of an electronic module or modification of a wiring harness—the impact on EMC can be assessed virtually through the digital twin, allowing appropriate measures to be taken without requiring complete physical tests. This approach will greatly improve development efficiency and may eventually enable simulation results to be used directly for compliance assessments.

2.6.2 AI-assisted Modeling and Optimization

Artificial intelligence(AI) will play an increasingly important role in EMC simulation[33]. On the one hand, machine learning can be applied to quickly establish equivalent models: by learning from large datasets of simulations and experiments, AI can automatically extract equivalent electromagnetic characteristics of complex components or systems, reducing the need for manual parameter tuning. On the other hand, AI can also be integrated into design optimization: simulation software can employ algorithms to automatically adjust factors such as wiring layouts, filter parameters, and grounding strategies to achieve optimal EMC performance. Some studies have already demonstrated AI models capable of simulating the heuristic rules used by EMC experts, providing targeted recommendations for interference suppression based on simulation results. This intelligence will enable engineers to explore the design space more efficiently, balancing EMC with other design goals such as weight, cost, and overall performance.

2.6.3 Broader Spectrum and Multi-field Coupling

Future automotive EMC challenges will span an ultra-wide spectrum from kilohertz to hundreds of gigahertz[34]. For example, wireless charging and power electronics primarily generate low-frequency high-current interference, while 5G and Vehicle-to-Everything(V2X) communication introduce electromagnetic environments in the millimeter-wave band. Simulation tools will therefore need to remain reliable across wider frequency ranges and support joint simulations of electromagnetic fields with other physical domains such as circuits, mechanics, and thermal processes. Furthermore, new interference mechanisms from autonomous driving sensors (radar, lidar, etc.) and high-voltage powertrains in electric vehicles will require new models and algorithms. It is foreseeable that EMC simulation software will evolve toward integrated platforms, providing end-to-end solutions from the chip level to the vehicle level, with the ability to automatically switch between algorithms suited to different application scenarios in order to balance efficiency and accuracy.

In short, the development of automotive EMC simulation is driving vehicle EMC engineering from an experience-driven approach toward a model-driven paradigm. While complete replacement of physical measurements with simulation will take time, the role of simulation in the development process will undoubtedly continue to grow. In the near future, as credibility improves and industry recognition accumulates, simulation-based compliance certification pilots are expected to emerge. For OEMs and component suppliers, mastering EMC simulation technology will become a core competence for enhancing research and development efficiency and ensuring EMC compliance of products.

3

Methods

3.1 Study Design and Workflow

This study follows an integrated workflow (see Fig. 3.1)that combines experimental EMC testing and numerical simulation in order to evaluate and predict the electromagnetic performance of an automotive wiper drive system. The overall objective is to establish a reliable methodology for correlating component-level results with vehicle-level behavior. The research process was divided into the following stages:

1. **Component-level EMC testing:** Testing of the wiper motor and controller in a SAC, including conducted and radiated emission measurements in accordance with CISPR 25.
2. **Numerical model development:** Creation of component-level numerical models in CST Studio Suite. Simulation parameters such as excitation sources and boundary conditions were refined using measured data.
3. **Comparison and correlation analysis:** Measured and simulated results were compared using error metrics such as frequency-domain deviations, Root Mean Square Error(RMSE), and correlation coefficients.
4. **Vehicle-level EMC simulation:** Simplified but representative models of the motor, wiring harnesses, and vehicle body structures were developed. Reference was made to ECE R10 requirements for geometry and frequency coverage.
5. **Iterative refinement and optimization:** Discrepancies between simulation and measurement were analyzed, and the models were improved accordingly.

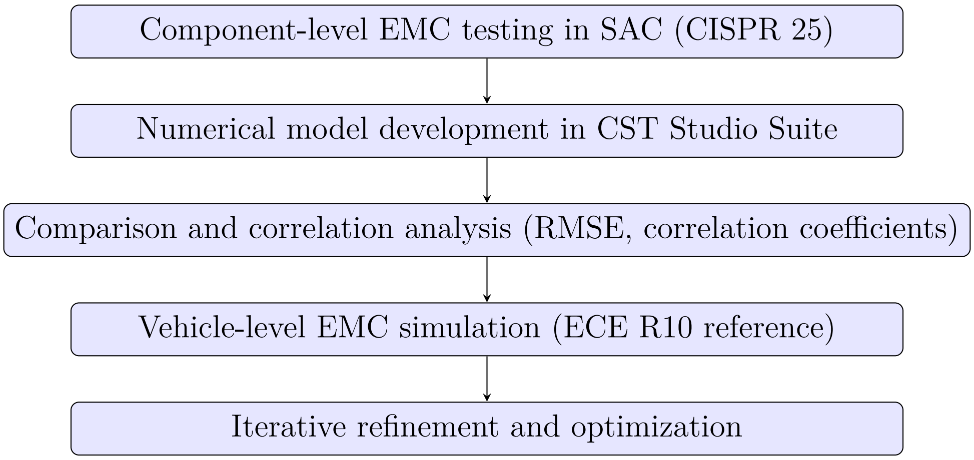

Figure 3.1: Workflow of EMC testing and simulation methodology.

This staged methodology is designed to progressively bridge the gap between controlled laboratory testing and full-vehicle EMC performance prediction.

4

Component-level test

4.1 Device Under Test (DUT): Front Wiper Motor

The device under test (DUT) is a 12 V DC brushed front wiper motor with an integrated smart driver. Control is via LIN 2.1 in accordance with ISO 17987. The motor exposes a four-pin connector carrying battery supply, chassis return, a LIN data line, and a vendor programming pin. In this study, pin 3 (programming) was intentionally left unconnected. Two operating states were exercised: *Mode ON* (electronics enabled, motor not wiping) and *High Speed* (electronics enabled, motor wiping at the high-speed setting). Fig. 4.1 shows the DUT connector layout and the functional assignment of the four pins. Table 4.1 elaborates the functions of connector pins; pin 3 is unused.

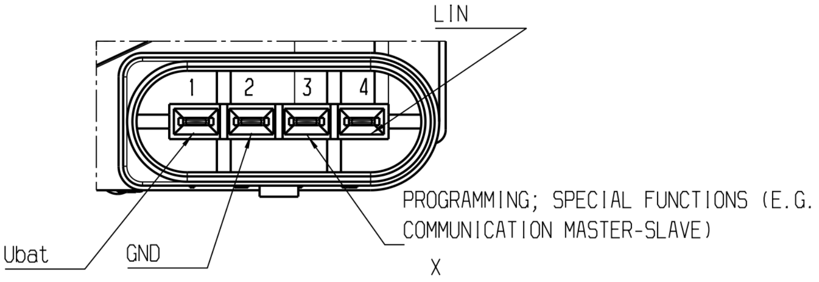

Figure 4.1: Connector and functional pins of the front wiper motor.

Table 4.1: Connector pin functions (four-pin interface).

Pin	Name	Function / Notes
1	Ubat	Battery supply (nominal 12 V).
2	GND	Chassis return.
3	PROG	Programming / special functions; *not connected in this campaign.*
4	LIN	LIN 2.1 data line (ISO 17987).

Fig. 4.2 shows the circuit connection diagram used to interface the DUT during the component-level tests.

Table 4.2: Operating states exercised in component-level tests.

State	Motor	Notes
Mode ON	Not wiping	Electronics enabled; H-bridge idle; LIN active.
High Speed	Wiping (high)	Electronics enabled; high-speed command via LIN.

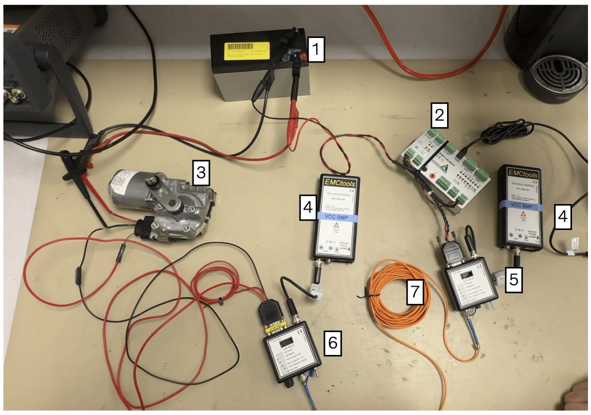

1.12V Battery
2. LIN Control
3. Wiper Motor (No Load)
4. Power Supply
5. Optical Transceiver (Master)
6. Optical Transceiver (Slave)
7. Optical Fiber

Figure 4.2: DUT circuit connection.

A dedicated load fixture was designed to ensure repeatability of testing. The wiring harness was arranged with a standardized spacing of 5 cm above a grounded reference plane, in compliance with CISPR 25 requirements. This ensured comparability with supplier data and allowed the results to be used directly as input for simulation modeling. Fig. 4.3 and Fig. 4.4 present the designed load fixture and its corresponding physical prototype used to ensure repeatable measurements.

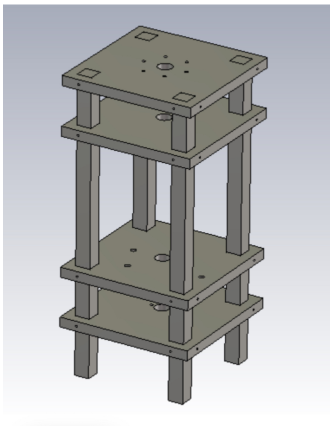

Figure 4.3: Load fixture design model.

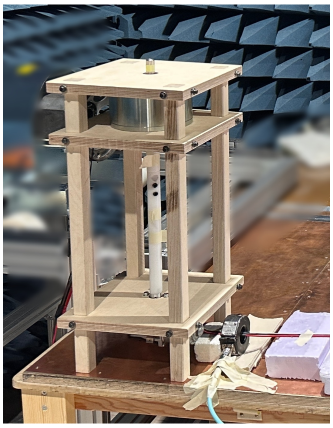

Figure 4.4: Load fixture prototype.

4.2 Measurement Framework

4.2.1 Site and Setup

Measurements were performed in a semi-anechoic chamber of approximately 6 m × 4 m × 3 m. The bench height was 0.90 m and the tabletop consisted of a well-bonded copper plate of 2.5 m × 2.0 m with 2 mm thickness. The front wiper motor (DUT) was bolted to the lower deck of a wooden rig; a current-controlled hysteresis brake providing a constant mechanical load of 4 Nm was bolted to the upper deck. A plastic shaft mechanically coupled the two units while maintaining electrical insulation. The motor housing was electrically floating with respect to the copper plane. Power was supplied by a lead-acid battery through an automotive LISN (Schwarzbeck NNBM 8124–400 implementing the CISPR 16/25 $(5\ \mu\text{H}+1\ \Omega) \parallel 50\ \Omega$ network). Control commands were sent from outside the chamber via an optical link to the LIN 2.1 interface. As seen in Table 4.2, two operating states were exercised: *Mode ON* (electronics enabled, motor not wiping) and *High Speed* (electronics enabled, motor wiping at the high-speed setting).

4.2.2 Harness Layouts and Antenna Geometry

Three layouts were used. For CE_3 (conducted current) the wiring harness was laid as a straight 2 m lead maintained at 5 cm above the plane and 20 cm from the table edge; the RF current probe was placed at 50 mm away from the DUT. For RE_2 (magnetic field) and RE_3 (electric field) the harness formed a “U” shape with a 1.5 m long side and two 25 cm returns, kept at the same height and edge clearance. Field probes and antennas were placed at 1 m away from the long side. RE_2 measurements were taken in two orthogonal loop orientations (denoted X and Y). RE_3 measurements were taken in horizontal and vertical polarisations.

Fig. 4.5 shows the CE_3 measurement setup and the corresponding harness and probe placement.

Figure 4.5: CE_3 measurement setup.

Fig. 4.6 and Fig. 4.7 show the RE_2 measurement setups with the magnetic loop antenna in the two orthogonal orientations (X and Y).

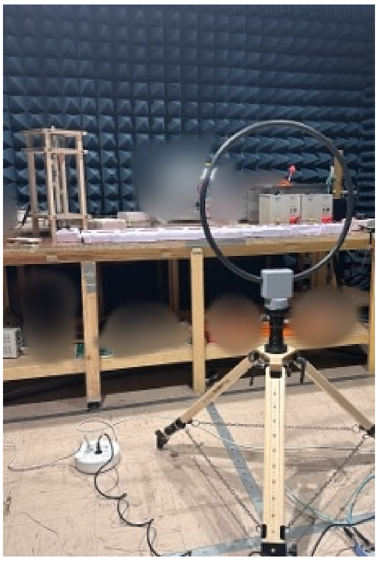

Figure 4.6: RE_2 setup, magnetic loop antenna in orientation X.

Figure 4.7: RE_2 setup, magnetic loop antenna in orientation Y.

Fig. 4.8 shows the monopole antenna arrangement used for RE_3 measurements in the 100 kHz–30 MHz band.

Figure 4.8: Monopole antenna measurement, 100 kHz – 30 MHz

Fig. 4.9 and Fig. 4.10 show the biconical antenna arrangements used for RE_3 measurements in horizontal and vertical polarisations over 30–200 MHz.

Fig. 4.11 and Fig. 4.12 show the log-periodic antenna arrangements used for RE_3 measurements in horizontal and vertical polarisations over 200–1000 MHz.

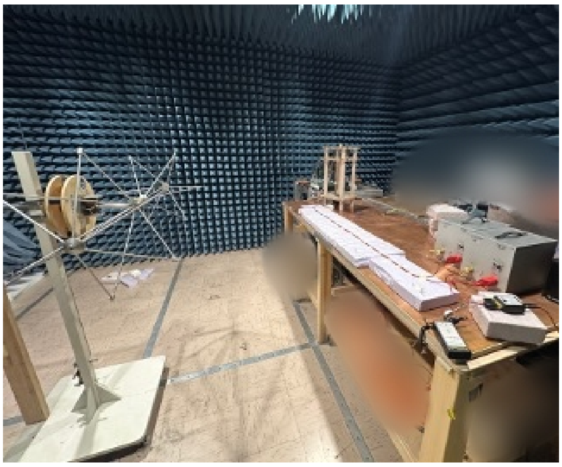

Figure 4.9: Biconical antenna in horizontal polarisation measurement, 30 - 200 MHz.

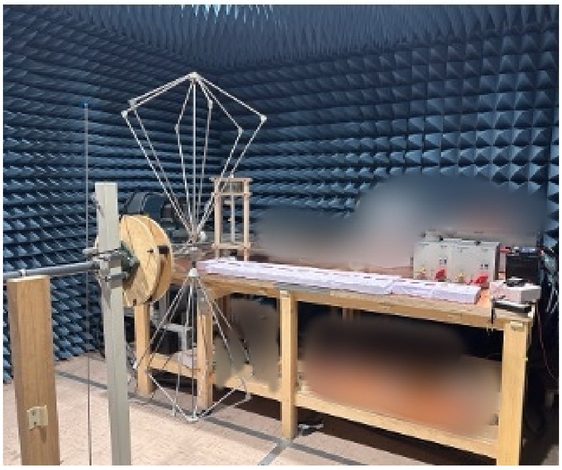

Figure 4.10: Biconical antenna in vertical polarisation measurement, 30 - 200 MHz.

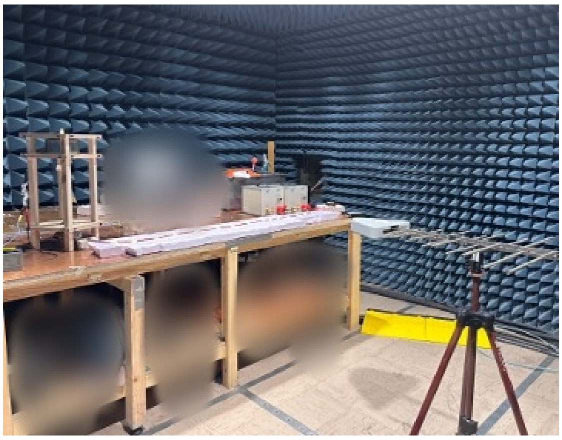

Figure 4.11: Log-periodic antenna in horizontal polarisation measurement, 200 - 1000 MHz.

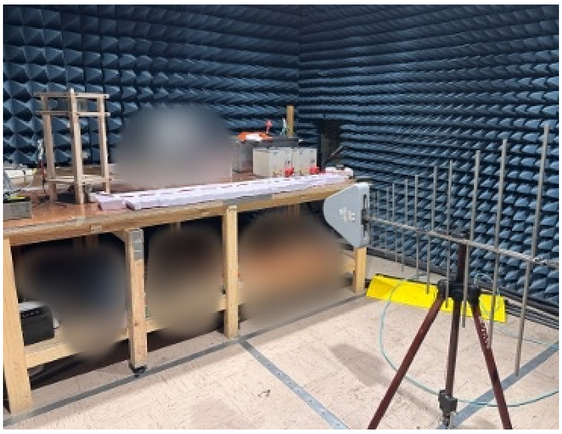

Figure 4.12: Log-periodic antenna in horizontal polarisation measurement, 200 - 1000 MHz.

Table 4.3: Antennas used in the EMC measurements.

Antenna type	**Frequency range**
Magnetic Loop	150 kHz – 30 MHz
Monopole	100 kHz – 30 MHz
Biconical	30 MHz – 200 MHz
Log-periodic	200 MHz – 1000 MHz

4.2.3 Instrumentation

Conducted current CE_3 was measured with a clamp-on RF current probe (ETS–Lindgren 94111–1, 1 MHz–1 GHz) providing a 50 Ω N-female output. Typical transfer-impedance anchors were used for reduction (about 0.9 Ω at 1 MHz, 2.5 Ω at 10 MHz, 5.0 Ω at 100 MHz, and 5.6 Ω at 500 MHz). The LISN in the power chain was a Schwarzbeck NNBM 8124–400, it provided the standardised supply network for conducted tests and a common RF reference.

All used antennas are listed in Table 4.3. Magnetic-field RE_2 in the LF–HF range employed a broadband active loop (R&S® HFH2–Z2E, 8.3 kHz–30 MHz) with nominal 50 Ω output, a neary constant antenna factor of +20 dB/m over most of the band, and optional 10 dB attenuation for large-signal conditions. For the low-frequency portion of RE_3 (100 kHz–30 MHz), a low-noise active vertical monopole (Schwarzbeck VAMP 9243) was used with constant antenna factor +10 dB/m; the unit is battery powered and was mounted on a bonded counterpoise for repeatability. The VHF portion of RE_3 (30–200 MHz) used biconical antenna BBVK 9138 in the VHA 9103 balun/holder; the assembly is linearly polarised with cross-polarisation exceeding 20 dB and exhibits an antenna factor that varies smoothly from roughly 12 to 28 dB/m across the band. The upper VHF to UHF portion (200 MHz–1 GHz in this study) used a log-periodic dipole antenna (ETS–Lindgren Model 3147) with average VSWR around 1.25:1 and manufacturer-supplied antenna-factor and gain curves. All antennas were operated at 1 m spacing from the harness long side, device-specific certificates and curves are cited in Appendix A.

4.2.4 Signal Chain and Conversions

Field and current quantities were obtained from receiver voltages using standard conversions. Electric field strength followed

$$E_{\mathrm{dB}\mu\mathrm{V/m}} = V_{\mathrm{dB}\mu\mathrm{V}} + \mathrm{AF}_{\mathrm{dB/m}} \tag{4.1}$$

with antenna factors taken from the respective device documentation (constant AF for the active monopole antenna in the low band; tabulated AF for the biconical antenna within 30–200 MHz; calibrated AF curve for the LPDA in the high band). Magnetic field strength for the loop antenna followed

$$H_{\mathrm{dB}\mu\mathrm{A/m}} = V_{\mathrm{dB}\mu\mathrm{V}} + \mathrm{AF}_{\mathrm{dB(1/m)}} \tag{4.2}$$

and common-mode current from the clamp probe followed

$$I_{\mathrm{dB}\mu\mathrm{A}} = E_{\mathrm{S,dB}\mu\mathrm{V}} - Z_{\mathrm{T,dB}\Omega} \tag{4.3}$$

Where present, preamplifier gain and coaxial cable loss were included in the reductions for the affected bands. Manufacturer sensitivity and linearity guidance for the active sensors was observed to avoid overload and to verify the measurement floor.

4.2.5 Background Noise

Background spectra were recorded with both DUT power and control signal off, while the brake current source remained on. Background curves are overlaid with all measurement plots for comparison. Frequency points where the background exceeded the measured level were flagged and excluded from quantitative indicators (e.g., RMSE and coverage), but retained in figures to document the floor.

4.2.6 Frequency Sampling and KPI Alignment

All spectra are reported on their native frequency grids. For pointwise comparisons and derived indicators (difference $\Delta(f)$, RMSE, and coverage), the comparison curve was aligned to the target grid by linear interpolation on a logarithmic frequency axis. Plotted data were not resampled.

4.2.7 Limits and Analysis Scope

Limits and compliance margins follow the shared definitions in Section 5.4, with margins computed as

$$\mathrm{Margin}(f) = \mathrm{Limit}(f) - \mathrm{Level}(f) \tag{4.4}$$

To capture potential higher-order resonances, CE_3 spectra were swept from 150 kHz to 320 MHz. Unless stated otherwise in Sections 4.3 and 4.5, quantitative indicators were reported over 150 kHz–30 MHz, whereas 30–320 MHz was presented for completeness and discussed qualitatively due to the low salience of high-frequency content in this setup.

4.3 CE3 Measurement Results

The conducted emission current (CE_3) of the wiper motor module was measured in the frequency range over 150 kHz–320 MHz, following CISPR 25 procedures. Both peak (PK) and average (AVG) detectors were applied. Two operating conditions were investigated: *High Speed* and *Mode ON*. For reference, background noise was recorded with the device disconnected. In all plots, four traces are provided: background PK, background AVG, measured PK and measured AVG.

Fig. 4.13 and Fig. 4.14 show the measured CE_3 spectra under *High Speed* and *Mode ON* operation, including the corresponding background and detector traces. Distinct spectral components appear near the commutation frequency and its harmonics in the low-frequency region (below 10 MHz), with broadband contributions extending beyond 30 MHz. Across the band, the background trace remains below the AVG/PK traces, indicating that the observed emissions originate from the DUT. The separation between PK and AVG reflects the pulsed nature of the emissions. Compared with *High Speed* operation, absolute current levels are reduced in *Mode ON*, while narrowband peaks remain visible at lower frequencies. The AVG trace lies notably below PK over most of the band, consistent with intermittent or burst-like behaviour.

To assess dataset consistency, the in-house measurements were compared with supplier-provided CE_3 data. The supplier report includes three conditions (background, *High Speed*, and *Mode ON*), each split into two sub-ranges: 150 kHz–108 MHz and

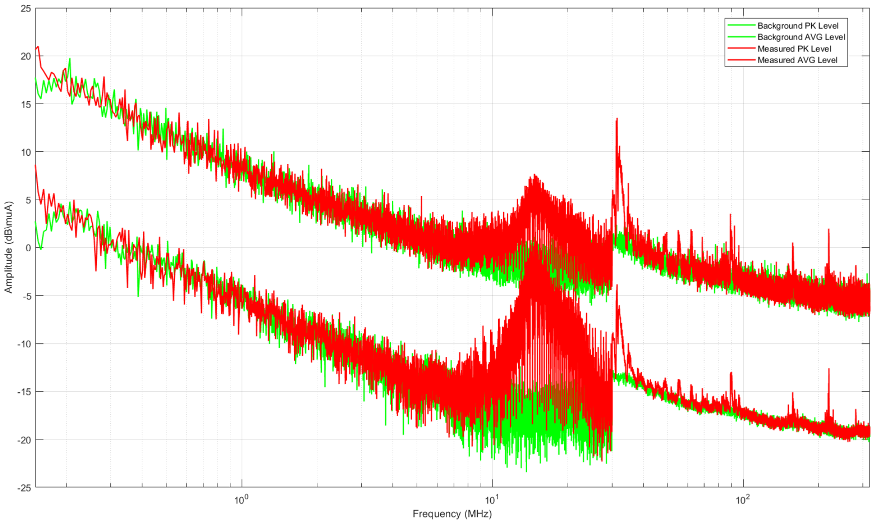

Figure 4.13: CE$_3$ spectra under *High Speed* operation (background PK, background AVG, measured PK and measured AVG).

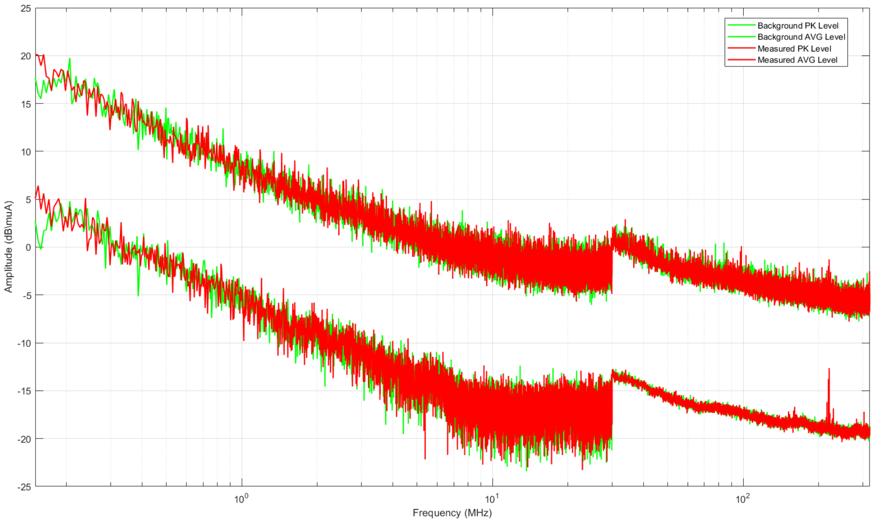

Figure 4.14: CE$_3$ spectra under *Mode ON* operation (background PK, background AVG, measured PK and measured AVG).

108–320 MHz. The corresponding figures are shown below in horizontally paired layouts for direct visual comparison.
Fig. 4.15, Fig. 4.16, and Fig. 4.17 show the supplier-provided CE_3 spectra for background, *High Speed*, and *Mode ON*, each presented in two frequency sub-ranges (150 kHz–108 MHz and 108–320 MHz) with AVG and PK.

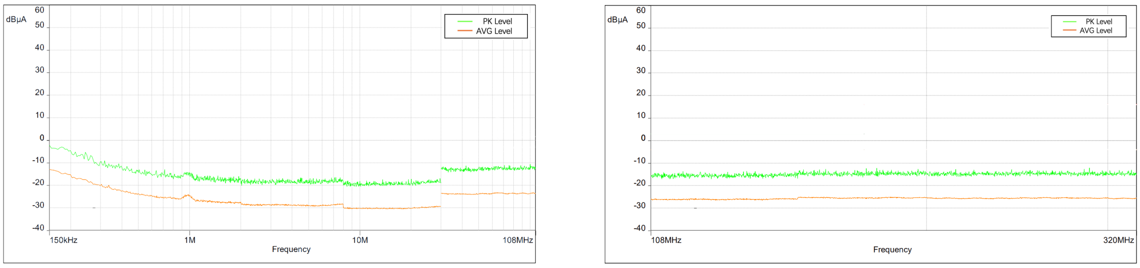

(a) 150 kHz–108 MHz

(b) 108–320 MHz

Figure 4.15: Supplier CE_3 background spectra in two frequency ranges (AVG and PK).

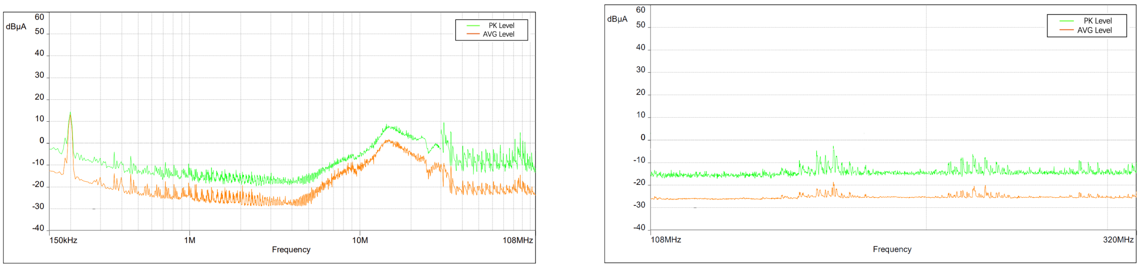

(a) 150 kHz–108 MHz

(b) 108–320 MHz

Figure 4.16: Supplier CE_3 *High Speed* spectra in two frequency ranges (AVG and PK).

Overall, the spectral distribution in both datasets is consistent, with characteristic peaks aligning in frequency. Differences in absolute magnitude can arise from chamber configuration, LISN/receiver settings (e.g., resolution bandwidth and dwell time), grounding topology, and cable routing.

4.4 RE2 Measurement Results

The radiated magnetic field (RE_2) of the wiper motor module was evaluated over 150 kHz–30 MHz in accordance with CISPR 25 procedures. Two orthogonal probe orientations (denoted as X and Y) were measured under two operating conditions: *High Speed* and *Mode ON*. For reference, background noise was recorded with the DUT disconnected. Unless otherwise noted, the in-house plots display background PK, background AVG, measured PK and measured AVG. The supplier report provides PK-only traces, this detector difference is acknowledged but does not affect the qualitative comparison below.

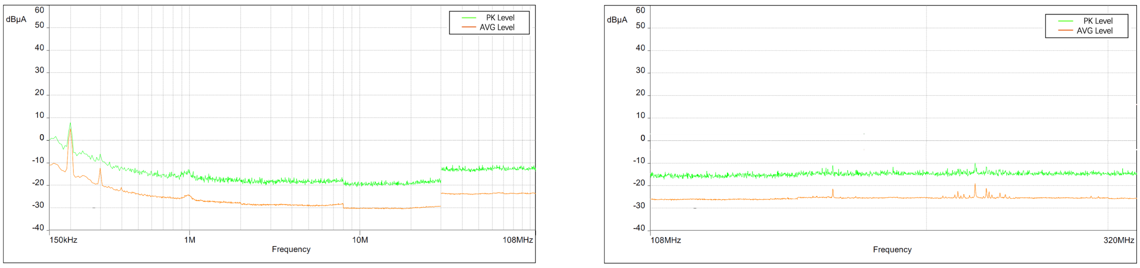

(a) 150 kHz–108 MHz **(b)** 108–320 MHz

Figure 4.17: Supplier CE_3 *Mode ON* spectra in two frequency ranges (AVG and PK).

4.4.1 In-house measurements

Fig. 4.18 and Fig. 4.19 show the in-house RE_2 spectra under *High Speed* and *Mode ON* operation for both X and Y probe orientations.

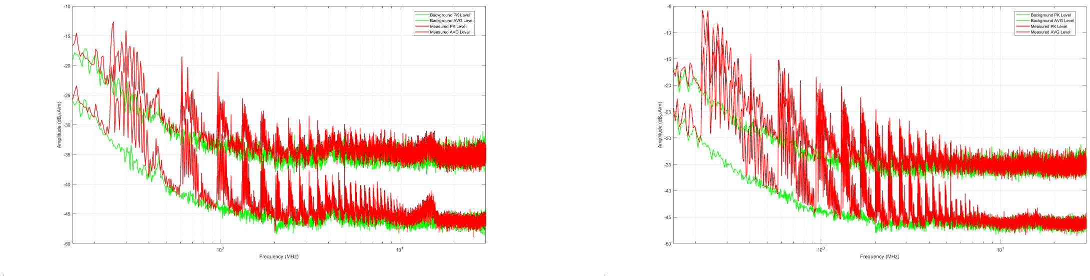

(a) X orientation **(b)** Y orientation

Figure 4.18: RE_2 spectra under *High Speed* operation (background PK, background AVG, measured PK and measured AVG).

Over most of the band the measured field remains close to the background, indicating that the overall magnetic radiation from the module is weak during steady rotation. Superimposed on this low baseline, periodic narrow spikes are visible. These spikes are not stationary in frequency: their positions depend on the receiver sweep timing relative to the motor's electrical/rotational state. In practice, the moment at which the sweep begins fixes the apparent spike locations across the entire trace, which reduces repeatability in terms of exact frequency placement.

4.4.2 On the origin and repeatability of the spikes

The periodic spikes observed in the *High Speed* plots are consistent with transient events associated with motor commutation and start-up segments that are intermittently captured by the sweeping receiver. Because the sweep is asynchronous with the motor state, the spike frequencies in the recorded spectra are effectively a sampling artifact of timing, rather than fixed narrowband emissions of the device. Consequently, exact spike frequencies are not strongly repeatable between runs with different sweep timing, even though the overall low emission baseline is

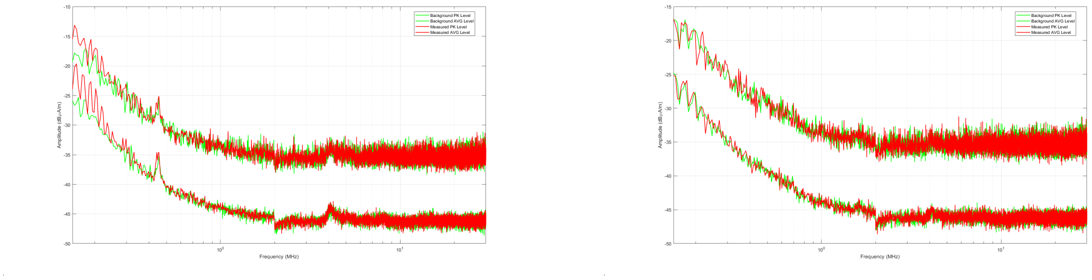

(a) X orientation

(b) Y orientation

Figure 4.19: RE$_2$ spectra under *Mode ON* operation (background PK, background AVG, measured PK and measured AVG).

repeatable. In subsequent simulation work we therefore do not attempt to reproduce these timing-dependent spikes; the focus is placed on steady, physically anchored spectral components.

4.4.3 Supplier report comparison

Fig. 4.20, Fig. 4.21, and Fig. 4.22 show the supplier-provided RE$_2$ spectra for background, *High Speed*, and *Mode ON* in both X and Y orientations (PK).

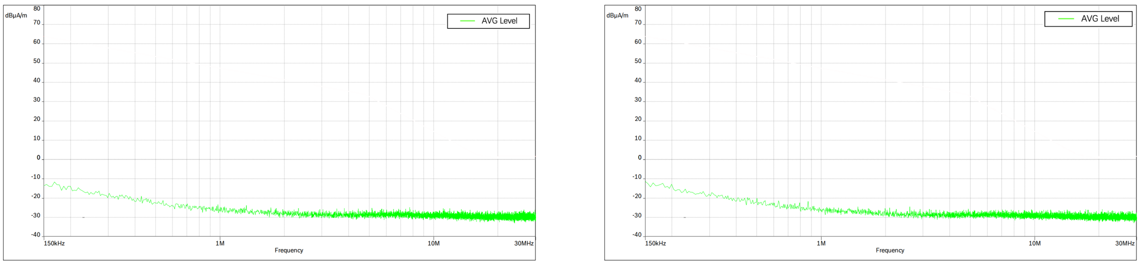

(a) Background, X orientation

(b) Background, Y orientation

Figure 4.20: Supplier RE$_2$ background spectra (PK).

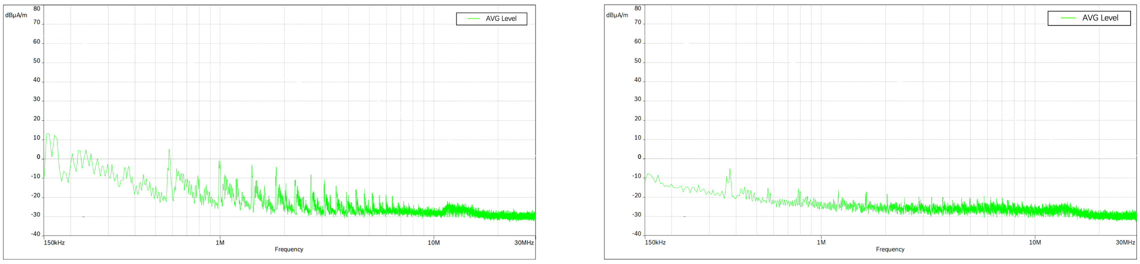

(a) High Speed, X orientation

(b) High Speed, Y orientation

Figure 4.21: Supplier RE$_2$ *High Speed* spectra (PK).

Overall, both datasets indicate that the module's radiated magnetic field during operation is weak and often indistinguishable from the background across most of

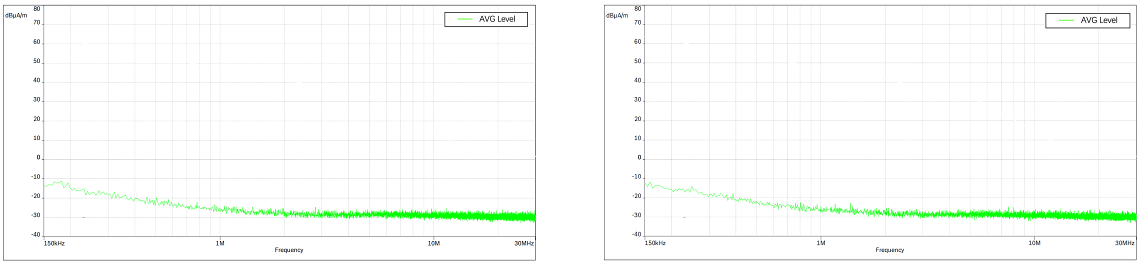

(a) Mode ON, X orientation

(b) Mode ON, Y orientation

Figure 4.22: Supplier RE_2 *Mode ON* spectra (PK).

the band. The narrow spikes seen in *High Speed* runs are timing dependent and not robust markers of device-intrinsic narrowband emissions, which explains their imperfect alignment between independent measurements.

4.5 RE3 Measurement Results

The radiated electric field (RE_3) of the wiper motor module was characterised over 100 kHz–1 GHz using three antenna/band combinations: monopole (100 kHz–30 MHz, vertical polarisation), biconical (30–200 MHz, horizontal/vertical polarisation), and log-periodic (200 MHz–1 GHz, horizontal/vertical polarisation). Two operating conditions were measured: *High Speed* and *Mode ON*. Unless otherwise noted, in-house plots contain background PK, background AVG, measured PK and measured AVG. Supplier RE_3 figures provide AVG and PK in the same plots.

4.5.1 In-house measurements

100 kHz–30 MHz (monopole) For readability in this low-frequency band, the AVG and PK traces are presented in separate figures for each operating condition. Fig. 4.23–Fig. 4.26 show the in-house RE_3 monopole spectra in the 100 kHz–30 MHz band for *High Speed* and *Mode ON*, with AVG and PK shown separately against the background.

In this band, the measured levels are clearly separated from the background over wide spans for both operating conditions, indicating measurable low-frequency radiation linked to commutation-related current loops and supply modulation. The AVG–PK difference reflects the pulsed nature of the emissions.

30–200 MHz (biconical). In the 30–200 MHz range, the measured spectra remain close to the background for both operating conditions. For horizontal polarisation, the AVG and PK traces almost completely coincide with the background across the entire band. For vertical polarisation, a slight excess above the background is observed only between 30 and 40 MHz, whereas above 40 MHz the measured levels again collapse onto the background, indicating no clearly resolvable emission margin at higher frequencies.

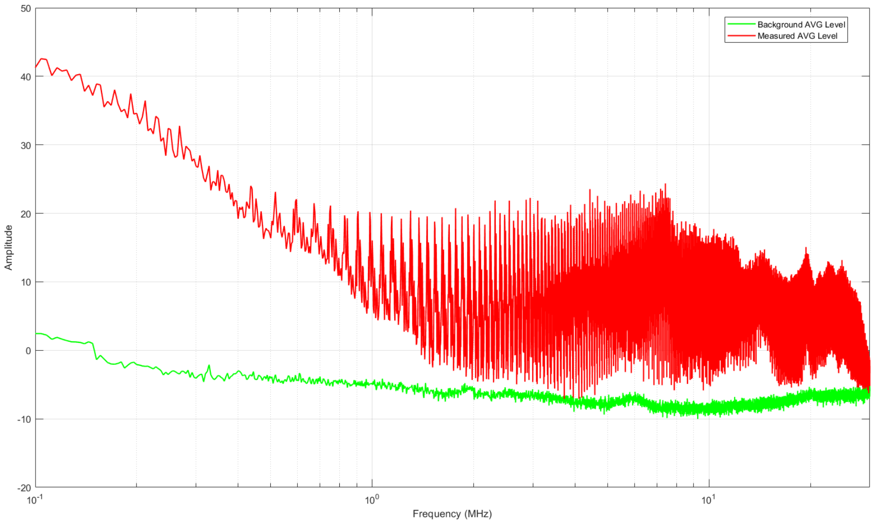

Figure 4.23: RE_3, 100 kHz–30 MHz (monopole), *High Speed*, AVG vs. background.

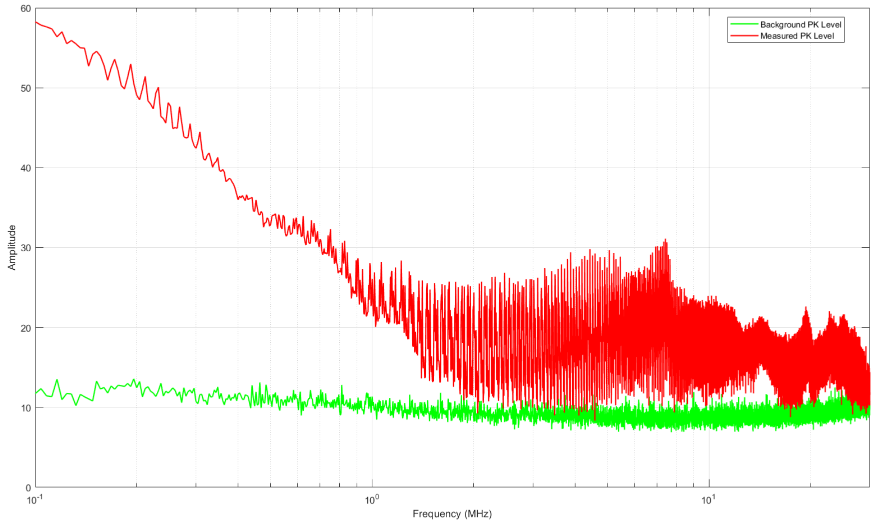

Figure 4.24: RE_3, 100 kHz–30 MHz (monopole), *High Speed*, PK vs. background.

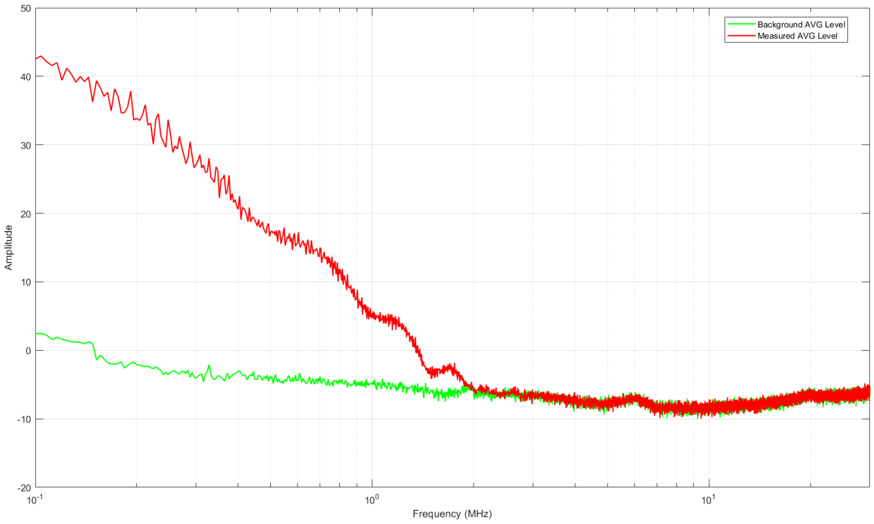

Figure 4.25: RE_3, 100 kHz–30 MHz (monopole), *Mode ON*, AVG vs. background.

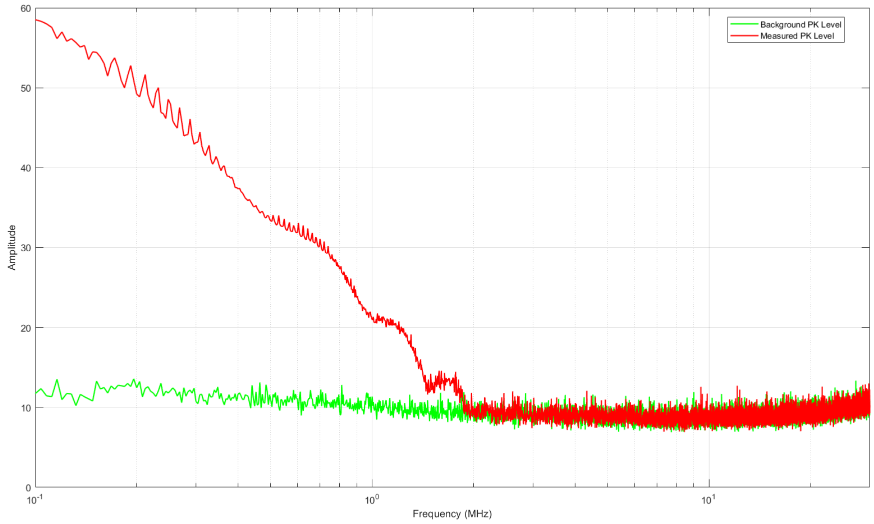

Figure 4.26: RE_3, 100 kHz–30 MHz (monopole), *Mode ON*, PK vs. background.

Fig. 4.27 and Fig. 4.28 show the in-house RE_3 biconical spectra in the 30–200 MHz band for *High Speed* and *Mode ON* in both horizontal and vertical polarisations.

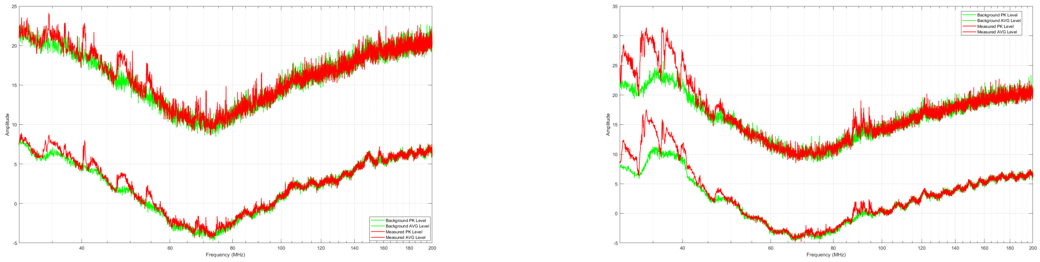

(a) Horizontal polarisation **(b)** Vertical polarisation

Figure 4.27: RE_3, 30–200 MHz (biconical), *High Speed* (background PK, background AVG, measured PK and measured AVG).

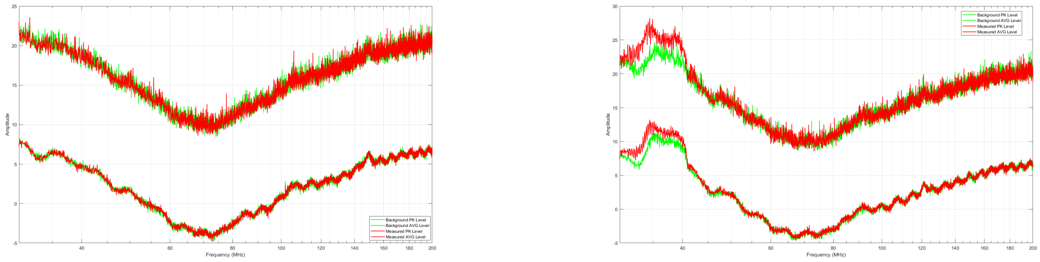

(a) Horizontal polarisation **(b)** Vertical polarisation

Figure 4.28: RE_3, 30–200 MHz (biconical), *Mode ON* (background PK, background AVG, measured PK and measured AVG).

200 MHz–1 GHz (log-periodic). Fig. 4.29 and Fig. 4.30 show the in-house RE_3 log-periodic spectra in the 200 MHz–1 GHz band for *High Speed* and *Mode ON* in both horizontal and vertical polarisations.

Across 200 MHz–1 GHz (log-periodic antennas measurement range), the spectra largely overlap with the background for both polarisations and operating conditions, indicating that high-frequency electric-field radiation is weak under the test setup.

4.5.2 Supplier report comparison

Supplier RE_3 figures (AVG and PK in the same plots) corroborate these observations across bands and operating conditions: pronounced separation from the background in 100 kHz–30 MHz, and nearly overlap with the background noise in 30 MHz–1 GHz. Fig. 4.31–Fig. 4.39 show the supplier-provided RE_3 spectra across bands and operating conditions, with AVG and PK shown together for each antenna and polarisation.

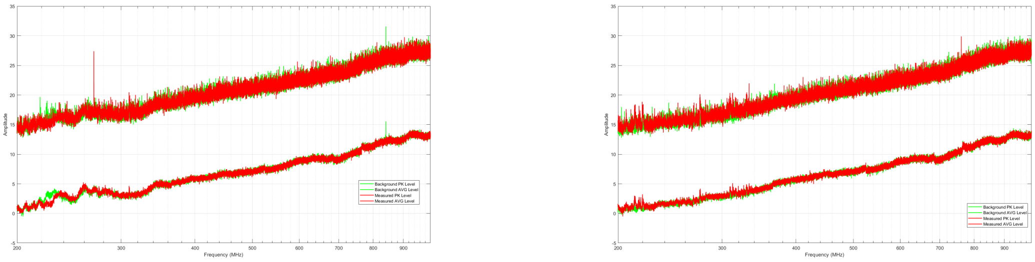

(a) Horizontal polarisation

(b) Vertical polarisation

Figure 4.29: RE$_3$, 200 MHz–1 GHz (log-periodic), *High Speed* (background PK, background AVG, measured PK and measured AVG).

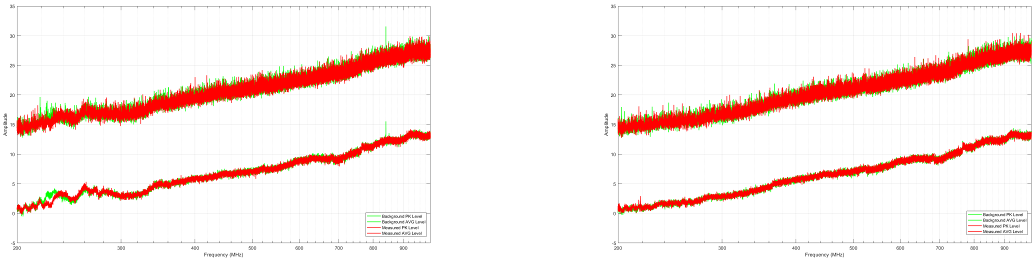

(a) Horizontal polarisation

(b) Vertical polarisation

Figure 4.30: RE$_3$, 200 MHz–1 GHz (log-periodic), *Mode ON* (background PK, background AVG, measured PK and measured AVG).

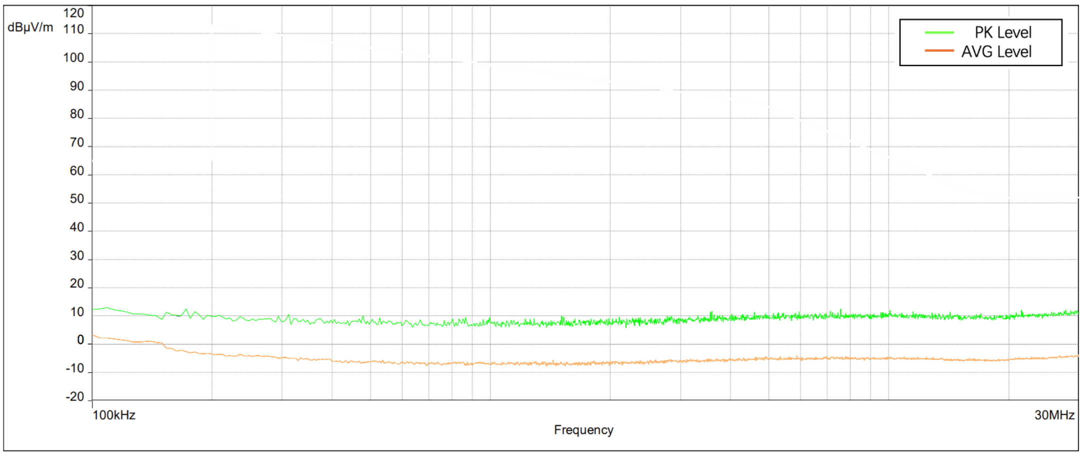

Figure 4.31: Supplier RE$_3$ background, 100 kHz–30 MHz (monopole; AVG and PK).

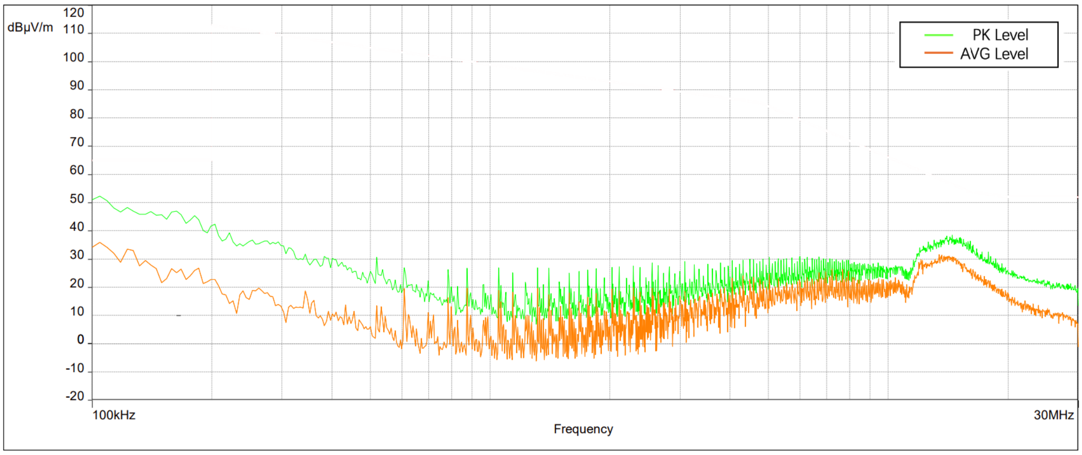

Figure 4.32: Supplier RE$_3$, 100 kHz–30 MHz (monopole; *High Speed*; AVG and PK).

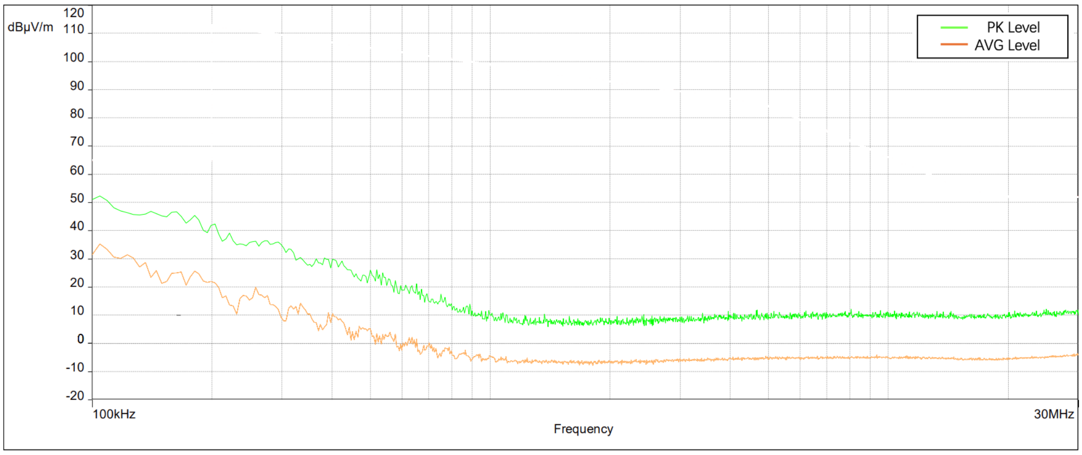

Figure 4.33: Supplier RE$_3$, 100 kHz–30 MHz (monopole; *Mode ON*; AVG and PK).

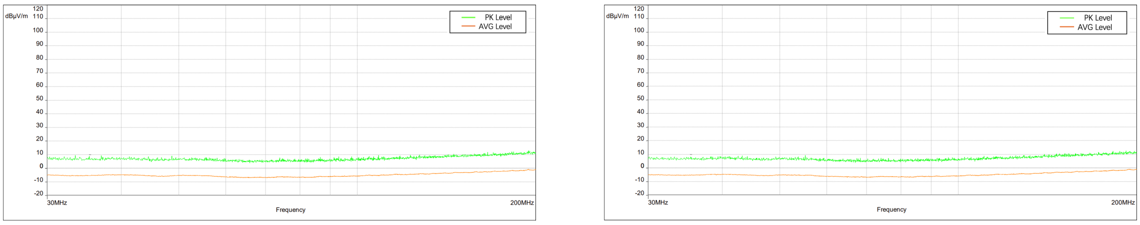

(a) Horizontal polarisation

(b) Vertical polarisation

Figure 4.34: Supplier RE$_3$ background, 30–200 MHz (biconical; AVG and PK).

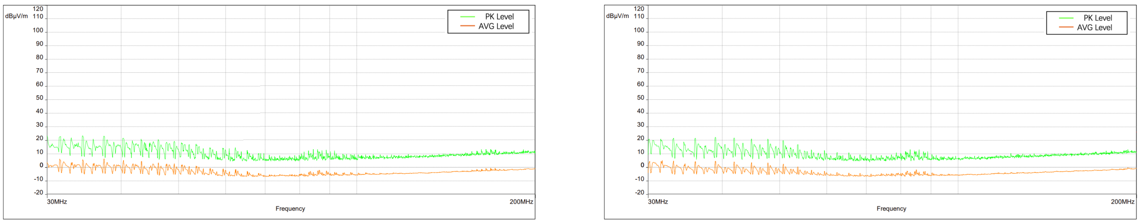

(a) Horizontal polarisation

(b) Vertical polarisation

Figure 4.35: Supplier RE_3, 30–200 MHz (biconical; *High Speed*; AVG and PK).

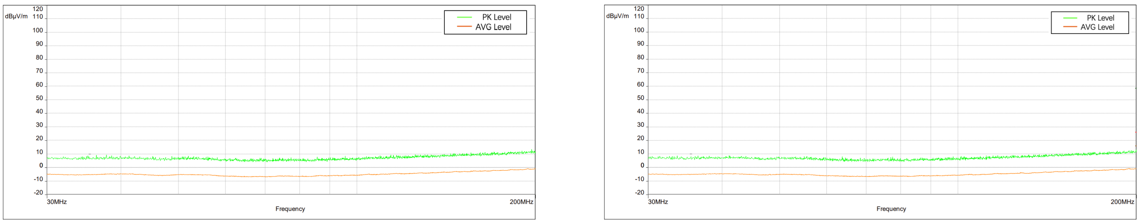

(a) Horizontal polarisation

(b) Vertical polarisation

Figure 4.36: Supplier RE_3, 30–200 MHz (biconical; *Mode ON*; AVG and PK).

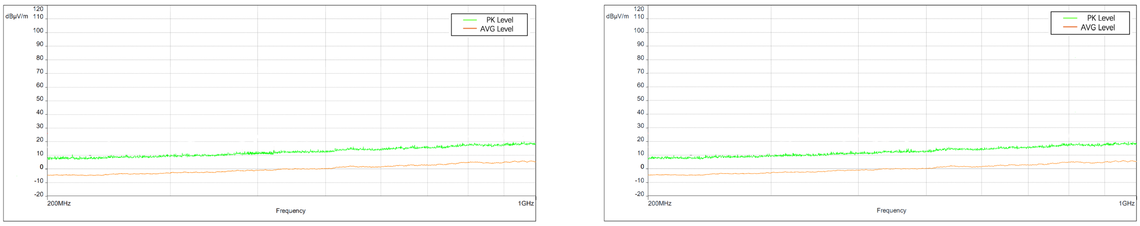

(a) Horizontal polarisation

(b) Vertical polarisation

Figure 4.37: Supplier RE_3 background, 200 MHz–1 GHz (log-periodic; AVG and PK).

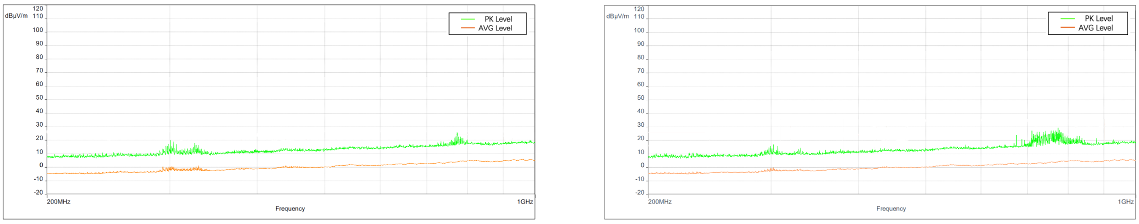

(a) Horizontal polarisation

(b) Vertical polarisation

Figure 4.38: Supplier RE_3, 200 MHz–1 GHz (log-periodic; *High Speed*; AVG and PK).

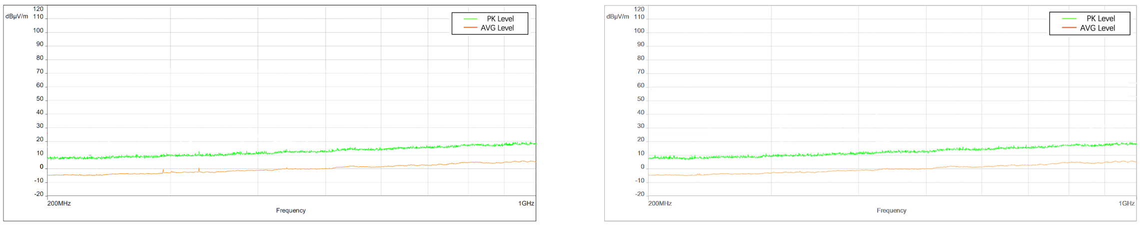

(a) Horizontal polarisation

(b) Vertical polarisation

Figure 4.39: Supplier RE_3, 200 MHz–1 GHz (log-periodic; *Mode ON*; AVG and PK).

4.5.3 Implications for subsequent simulation

Given the pronounced signals separated from the background noise in the 150 kHz–30 MHz band and those signals nearly overlapped with the background noise across 30 MHz–1 GHz, subsequent modelling prioritises the electric-field behaviour in 150 kHz–30 MHz. High-frequency 30 MHz-1 GHz electric-field radiation is considered weak under the present setup and is therefore not the primary focus of the predictive modelling and correlation tasks in later chapters.

5

Component-level simulation

5.1 Objectives, Scope, and Simulation Overview

This chapter develops a component-level electromagnetic model that is *driven by measurement* and *faithful to the test geometry.* The measured common-mode (CM) conducted emission is used to excite the supply harness, and the resulting radiated fields are evaluated at the same probe/antenna locations as in Chapter 4. The approach deliberately abstracts the device-under-test (DUT) internal operation and concentrates computational effort on the dominant coupling paths formed by the harness, fixtures, ground reference, and receiving sensors. Unless otherwise stated, the evaluation focuses on 150 kHz to 30 MHz; the rationale for this band selection is discussed in Sec. 5.4.2.

5.1.1 Excitation Derived from Measured CE

The excitation is constructed from CM current spectra measured on the three conductors at a probe positioned 5 cm from the DUT, as reported in Chapter 4. Since only magnitudes are available, the simulation injects an *energy-equivalent* CM source with frequency-dependent amplitude $|I_{\mathrm{CM}}(f)|$ consistent with the detector settings used in the test campaign. Section 5.2.4 specifies how the background-subtracted, root-sum-square combination across the three conductors is mapped to the driven ports.

5.1.2 Model Boundary and Comparison Protocol

The computational domain emulates the anechoic-chamber environment used for testing; absorbing terminations suppress spurious reflections within the band of interest. Simulated fields are sampled at the measurement locations and converted to the same units. Background handling, detector alignment, and quantitative metrics for agreement (median error, 90th-percentile error, band RMSE, and hit rate within a $\pm X$ dB corridor) follow the definitions in Secs. 4.2.5 and 4.2.6.

5.2 Electromagnetic Modeling Methodology

5.2.1 Geometry Sources and Coordinate System

All three-dimensional entities reproduce the laboratory layout used for the measurements. The anechoic chamber is modeled as a 6 m × 4 m × 3 m rectangular domain. A wooden table of height 0.94 m supports a copper tabletop of 2.5 m × 2.0 m with thickness 2 mm. The tabletop is bonded to the chamber ground through four copper straps 10 cm wide and 2 mm thick to ensure a low-impedance return path.

The supply harness follows a U-shaped route with a total length of approximately 2 m, composed of two 0.25 m legs and a 1.5 m center segment. The long segment runs parallel to the table edge with an inward offset of 0.10 m and is laterally centered. The two short legs are orthogonal to the long segment. Bend radii are 10 mm. Foam spacers, modeled as vacuum, maintain a height of 50 mm above the copper plate along the supply harness.

The receiving antenna is a vertical monopole: an aluminum rod of diameter 15 mm and height 104 cm mounted on a 0.60 m × 1.20 m, 2 mm-thick aluminum base plate conductively bonded to the copper tabletop. The antenna is centered along the table edge, located 0.90 m from the edge and 1.00 m from the long harness segment.

The DUT enclosure is mechanically floating above the tabletop. It does not touch the copper plate. The only intentional reference to ground is the dedicated ground lead, which emphasizes the low-frequency common-mode return through the harness–ground system. Fig. 5.1 shows the complete 3D (three-dimensional) model used in the component-level simulation.

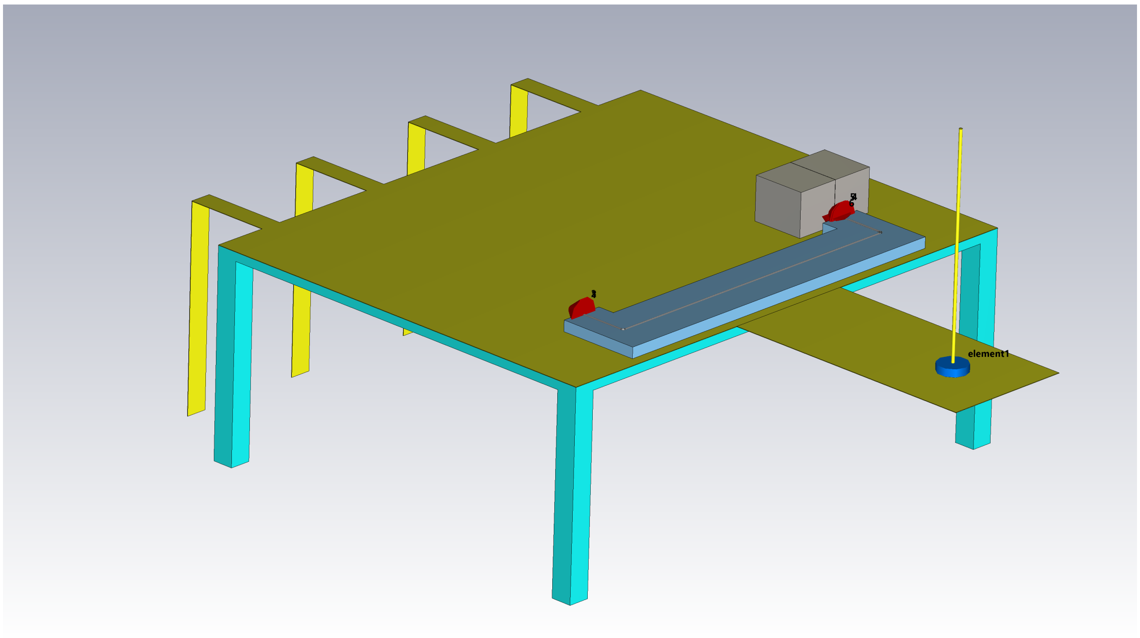

Figure 5.1: Complete three-dimensional model used in the component-level simulation, including chamber, table and copper plate, DUT, harness, LISNs, and the receiving antenna.

5.2.2 Material Models

Electromagnetic properties are specified for the frequency range of interest. The copper tabletop and wire cores use non-magnetic copper with $\sigma_{\mathrm{Cu}} = 5.96 \times 10^7\,\mathrm{S/m}$ and $\mu_r = 1$. Aluminum parts use $\sigma_{\mathrm{Al}} = 3.56 \times 10^7\,\mathrm{S/m}$ and $\mu_r = 1$. Cable insulation is modeled as rubber with $\epsilon_r = 3$ and $\mu_r = 1$. The wooden table is represented by a fitted second-order dispersive permittivity with $\mu_r = 1$. Conductor dispersion is handled by the solver's surface-current formulation, and dielectric losses for rubber and wood follow the adopted material models.

5.2.3 Harness Parameterization

The harness consists of three insulated copper conductors without an overall shield, denoted as power, ground, and signal. The power and ground conductors have an outer diameter of 3.6 mm (including insulation) and a copper cross-section of 2.5 mm^2. The signal conductor has an outer diameter of 1.5 mm with a copper cross-section of 0.35 mm^2. The nominal center-to-center spacing between adjacent conductors is 5 mm. The three-dimensional routing, height above the tabletop, and bend radii follow Sec. 5.2.1.

5.2.4 Ports and CE-Driven Excitation

Six ports are defined according to the measurement wiring: (1) DUT positive, (2) DUT negative, (3) DUT signal, (4) LISN positive, (5) LISN negative, and (6) signal input to the optical transceiver. Ports 1–3 are driven by a common-mode current excitation constructed from the background-subtracted spectra at 5 cm from the DUT and formed by a root-sum-square combination across the three conductors. Because only magnitudes are available, an energy-equivalent amplitude prescription is used. Ports 4–5 connect the harness to the LISN networks. Port 6 is terminated with $50\,\Omega$. When co-simulation is enabled, the effective port impedances are governed by the circuit schematic and follow the network definition.

5.2.5 LISN Co-Model and Full Schematic

Two single-channel LISNs are used, one on the positive line and one on the negative line. In the measurements both units are configured to *50 Ω termination*, and the rear-panel *1 μF* capacitor is enabled. The LISN enclosures are modeled as full three-dimensional metallic solids using the external dimensions. Their internal networks are implemented in the schematic domain exactly as specified by the manufacturer, without additional parasitics or frequency-dependent amendments. The mapping between three-dimensional ports and circuit nodes enforces the common-mode impedance seen by the harness according to the datasheet topology. The complete simulation schematic, including all six ports (DUT+, DUT−, DUT signal, LISN+, LISN−, and receiver input), is shown in Fig. 5.2.

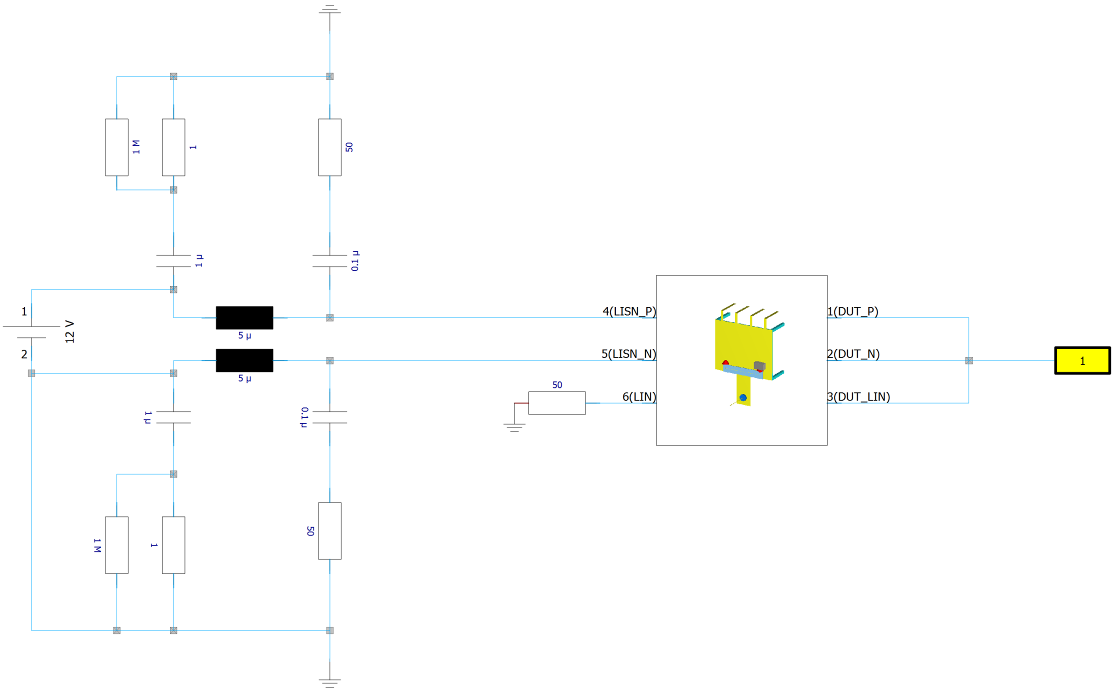

Figure 5.2: Complete co-simulation schematic with six ports: DUT positive, DUT negative, DUT signal, LISN positive, LISN negative, and optical transceiver input. The LISN networks follow the datasheet topology, port impedances are governed by the schematic.

5.2.6 Boundary Conditions and Chamber Emulation

The computational domain matches the chamber dimensions of 6 m × 4 m × 3 m. The bottom boundary serves as the global electric reference to emulate the chamber floor. All other faces are perfectly absorbing, providing reflection-free boundaries over 150 kHz to 30 MHz. The LISN chassis feet are modeled in direct conductive contact with the tabletop copper plate, consistent with the laboratory setup. Minimum clearances from radiating structures to the boundaries satisfy low-frequency stability rules and are verified in the convergence study.

5.2.7 Receiver Readout and Field Proxy

A 1 MΩ lumped element is placed at the antenna base to emulate the receiver input. The simulated voltage across this element is converted to field strength using the antenna factor. The antenna-factor table versus frequency is provided in the Appendix A.1.

5.3 Solver Configuration and Co-Simulation

5.3.1 Frequency Sweep and Convergence Criteria

A general-purpose interpolative broadband sweep is employed over the band of interest. The solver evaluates a minimal adaptive set of seven frequency samples, $\{0.15, 9.804, 15.075, 22.494, 26.220, 28.110, 30.000\}$ MHz, and generates a log–linear grid of 1001 points for reporting. Convergence is controlled by two broadband delta metrics with thresholds of 0.01 for all S-parameters and 0.05 for all probes. User-defined sampling entries not conforming to this plan are ignored by the solver, while the lower bound remains at 0.15 MHz.

Simulation frequencies are not strictly aligned to the measurement grid. No explicit modeling of Intermediate Frequency (IF) bandwidth or detector response is performed. For comparison, simulated observables are converted to the same units as the measurements and evaluated by curve similarity metrics as described in Sec. 5.3.5.

5.3.2 Field–Circuit Co-Simulation Topology

A field–circuit co-simulation couples the three-dimensional EM model with a circuit schematic so that the terminal conditions are enforced by the network definition. The LISN enclosures are resolved as 3D metallic solids to capture scattering and chassis parasitics, while their internal networks reside in the schematic domain; see Sec. 5.2.5 for configuration details. Port definitions and the CE-driven excitation follow Sec. 5.2.4 and are not reiterated here. The LISN chassis is bonded to the copper tabletop by direct metallic contact to reproduce the measurement return path.

5.3.3 Numerical and HPC Settings

The frequency-domain solver of CST Studio Suite with Version 2025.4 runs on 64-bit Windows system. Hyperthreading is disabled for parallel computations. Twelve CPU threads are used. Units are millimetres for geometry, megahertz for frequency, and seconds for time. Curved elements are enabled up to third order with automatic reduction to maintain mesh quality. Peak physical memory usage is 8.6 GB. The total wall-clock time for the broadband sweep is 360 s. Free disk space at the start is 695 GB. Solutions and meshes are not archived because coefficient backup is deactivated.

5.3.4 Meshing Strategy and Adaptive Refinement

An automatic tetrahedral mesh is employed. A representative initial mesh contains 218,768 tetrahedra with minimum edge length 0.229 mm, maximum edge length 4.45 mm, minimum element quality 8.47×10^{-4}, and average quality 0.347. Local refinements are enforced at ports, along wire surfaces, at connector shells and narrow gaps, at the DUT ground lead, and at the antenna feed to resolve surface-current gradients and near-field hot spots. Maximum step widths are constrained relative to conductor radii and gap dimensions. Multi-frequency convergence is assessed by the stability of port currents and impedances as well as sampled fields; threshold criteria are specified in Sec. 5.3.

Adaptive refinement proceeds in three passes initiated at 30 MHz. The cell count increases from 220,278 to 252,298, while the global S-parameter delta decreases from 0.1399 after the second pass to 0.0156 after the third, which meets the target accuracy and terminates adaptation. The solver reports an edge-length ratio of 1:1225 between the shortest and longest model edges and applies local curvature reduction where necessary to preserve element quality.

5.3.5 Reporting and Comparison Protocol

Receiver emulation and field conversion follow Sec. 5.2.7 and are not repeated here. Because IF bandwidth and detector behavior are not modeled, agreement is assessed by curve similarity on the measurement frequency grid after unit alignment consistent with the official report. Two band-wise measures are used: the Pearson correlation coefficient r and the normalized root-mean-square error

$$\mathrm{nRMSE} = \frac{\left(\sum_k (x_k - y_k)^2\right)^{1/2}}{\left(\sum_k y_k^2\right)^{1/2}}.$$

For each configuration, these metrics are reported together with descriptive statistics of the absolute deviation in dB.

5.3.6 Reproducibility Notes

The software version, unit system, boundary conditions, adaptive mesh refinement history, and resource usage are recorded above for traceability. The computational mesh is not locked; repeat runs reproduce the reported results by reusing the adaptive strategy and thresholds rather than a fixed mesh snapshot. The complete schematic is referenced in Fig. 5.2 and the full 3D model in Fig. 5.1.

5.4 Post-Processing and Comparison Protocol

5.4.1 Observable and unit alignment

The simulation reports the voltage across the 1 MΩ lumped element at the monopole antenna base. This voltage is converted to electric-field strength through the antenna factor (AF) using an additive relation in dB units:

$$E\,[\mathrm{dB}\,\mu\mathrm{V/m}] \;=\; V\,[\mathrm{dB}\,\mu\mathrm{V}] \;+\; AF\,[\mathrm{dB/m}]. \tag{5.1}$$

The AF is provided as a CSV table in the Appendix A.1. Since the AF grid and the simulation frequencies are not identical, a piecewise-linear interpolation in frequency is used to obtain $AF(f)$ at the simulation points. No extrapolation beyond the AF table bounds is performed; out-of-range points are omitted when generating plots.

5.4.2 Frequency range and scope of evaluation

The evaluation focuses on the electric field from 150 kHz to 30 MHz. Above 30 MHz the measured electric field curves are drowned out by the background noises, so additional modeling in that range offers limited diagnostic value. Magnetic-field measurements are not used for validation in this chapter. As discussed in Chapter 4 ("On the origin and repeatability of the spikes"), the periodic spikes visible in high-speed spectra originate from asynchronous sampling of motor-commutation transients; their exact frequencies are not strongly repeatable across runs. The simulations therefore do not attempt to reproduce such timing-dependent spikes and instead target steady, physically anchored spectral components.

5.4.3 Comparison protocol and evaluation style

The simulation and measurement frequency points are not strictly aligned, and no numerical modeling of IF bandwidth or detector response is applied. After unit alignment via (5.1), qualitative agreement is assessed by visual overlay and curve-shape similarity on the measurement grid obtained by resampling the simulated trace. Quantitative scores, such as the Pearson correlation coefficient and a normalized RMS difference, may be reported as descriptive aids but are not used as pass/fail criteria. Emphasis is placed on consistent trends, locations of spectral humps and nulls, and the ordering of levels between configurations, rather than pointwise errors.

5.4.4 Data flow and reproducibility

The post-processing pipeline is: background-subtracted common-mode current spectrum → field–circuit co-simulation → base-voltage readout → AF interpolation → electric-field curve. The AF CSV and the simulation frequency list are archived in the Appendix A.1 to support reproduction of the plotted results.

5.5 Results Overview and Notes on Interpretation

Fig 5.3 and Fig 5.4 present overlays of the simulated and measured electric-field spectra from 150 kHz to 30 MHz. Across the considered configurations, the simulations reproduce the principal spectral trends and the ordering of levels between harness placements and LISN settings. In the Mode-On case (Fig 5.3), the simulated AVG trace is nearly coincident with the measured AVG over broad sub-bands—most notably from the lower band edge up to mid-band—indicating that the measurement-derived excitation and the field–circuit coupling capture the dominant return paths. In the High-speed case (Fig 5.4), the overall envelope likewise agrees and the two AVG curves are nearly overlapping over large portions of the band. Where background dominance is evident near the upper band edge, discrepancies are not interpreted as model deficiencies.

When reported, the Pearson correlation and the normalized RMS difference are provided as descriptive indicators of shape similarity and are not used as pass/fail thresholds. Emphasis is placed on consistent trends, locations of spectral humps and nulls, and configuration-wise ordering rather than pointwise errors.

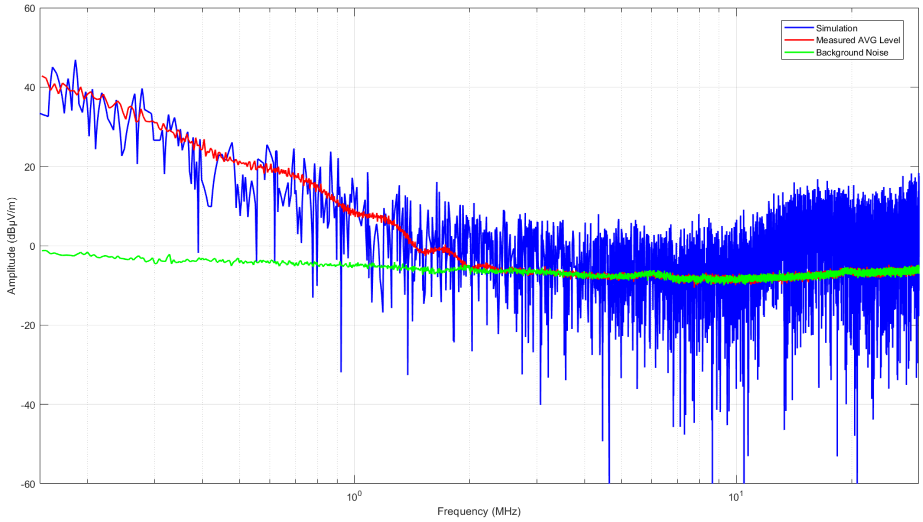

Figure 5.3: Mode-On condition: overlay of measured AVG, simulated AVG, and measured background noise, for 150 kHz to 30 MHz.

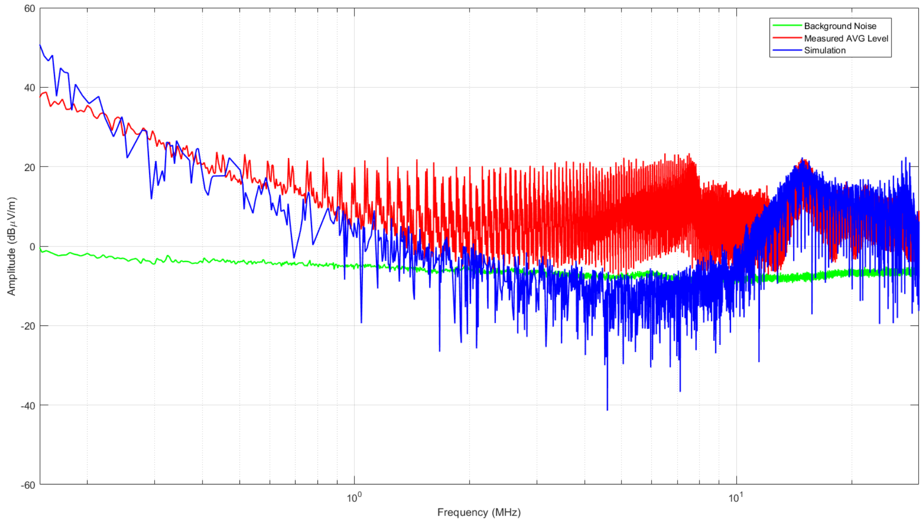

Figure 5.4: High-speed condition: overlay of measured AVG, simulated AVG, and measured background, for 150 kHz to 30 MHz.

5.6 Chapter Summary

This chapter established a measurement-driven, geometry-faithful component-level model, coupled to a LISN network via field–circuit co-simulation. The excitation is derived from background-subtracted common-mode currents, and the observable is the electric field obtained from the antenna receiver-base voltage through an interpolated antenna factor. Validation is intentionally qualitative: frequency points are not strictly aligned, detector and IF bandwidth are not modeled, and agreement is judged primarily by the similarity of spectral shapes in 150 kHz to 30 MHz. Timing-dependent spikes and magnetic-field measurements are excluded from the evaluation scope. The resulting workflow provides a stable, physically interpretable baseline for the vehicle-level extrapolations in Chapter 6.

6

Vehicle-Level Prediction

6.1 Objectives and Scope

This chapter presents a full-vehicle electromagnetic (EM) simulation intended to assess radiated fields in the 0.15 MHz to 320 MHz band and to identify engine-bay near-field hot spots. No vehicle-level measurements were performed in this project; therefore, all results in this chapter are reported as *mechanism-oriented predictions* and *relative comparisons* rather than validation-grade evidence. The excitation is consistent with Section 5.1: a common-mode (CM) source derived from conducted-emission measurements at the motor side.

6.2 Vehicle Model, Materials, and Boundaries

The three-dimensional model comprises the body-in-white (BIW) metallic frame, the wiper motor, the 12 V battery, the DC–DC converter, the fuse box, the Central Electronic Module (CEM), and the associated harness. All parts are imported from company-provided, preprocessed models with a *fixed* tetrahedral mesh.

As shown in Fig. 6.1, the wiring-level overview summarizes the functional interconnections among the wiper motor, the 12 V battery, the DC–DC converter, the fuse box, and the CEM, together with the principal harness routes and the return paths used in the simulations. Fig. 6.2 depicts the full three-dimensional electromagnetic model, indicating the body-in-white, the mounted subsystems, and the routed harness corridors.

To control computational cost, all conductive structures except the harness are modeled as perfect electric conductors (PECs), whereas the harness conductors use copper material properties *identical to Chapter 4*, i.e., $\sigma_{\mathrm{Cu}} = 5.96 \times 10^{7}\,\mathrm{S/m}$ and $\mu_r = 1$. All ground returns are realized as solid contacts at the physical mounting points on the BIW to mimic the real vehicle installation. Boundary conditions are open (absorbing) on $\mathrm{X}_{\mathrm{min/max}}$, $\mathrm{Y}_{\mathrm{min/max}}$, and $\mathrm{Z}_{\mathrm{max}}$; the $\mathrm{Z}_{\mathrm{min}}$ plane is set as the global electric reference. No geometrical symmetries are enabled. Units are millimetres for geometry, megahertz for frequency, and nanoseconds for time.

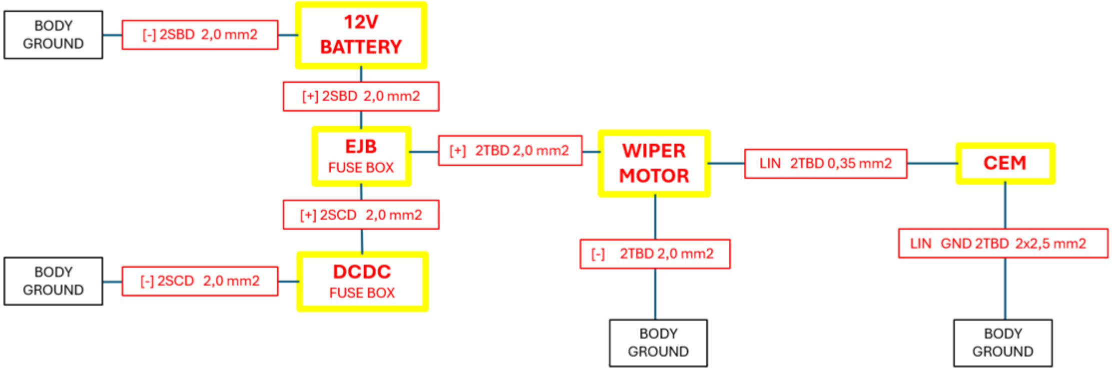

Figure 6.1: Connection overview (illustrative) of participating devices (motor, battery, DC–DC, fuse box, CEM) and their harness links in the simulation. This diagram is a functional wiring sketch *without* detailed equivalent circuits.

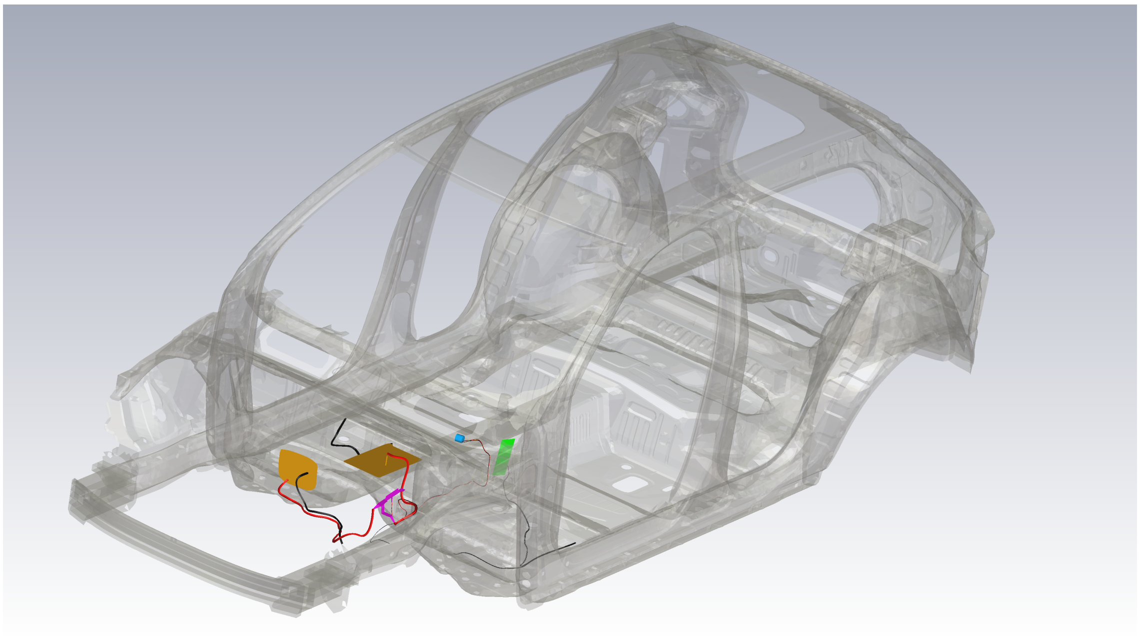

Figure 6.2: Full-vehicle 3D EM model.

6.3 Ports and Operating Modes

The port mapping follows the component-level model convention for traceability:

- Ports 1–3: motor-side terminals driven by the CE-derived CM source.
- Port 4: internal equivalent circuit of the 12 V battery.
- Port 5: internal equivalent circuit of the DC–DC converter.
- Port 6: signal input terminated to 50 Ω to ground.

Three supply scenarios are simulated in sequence: (i) battery-only, (ii) DC–DC-only, and (iii) dual supply. Figure 6.3 shows the precise port locations in the three-dimensional model; Figure 6.4 shows the corresponding ports in the circuit schematic and their connections in the equivalent circuit.

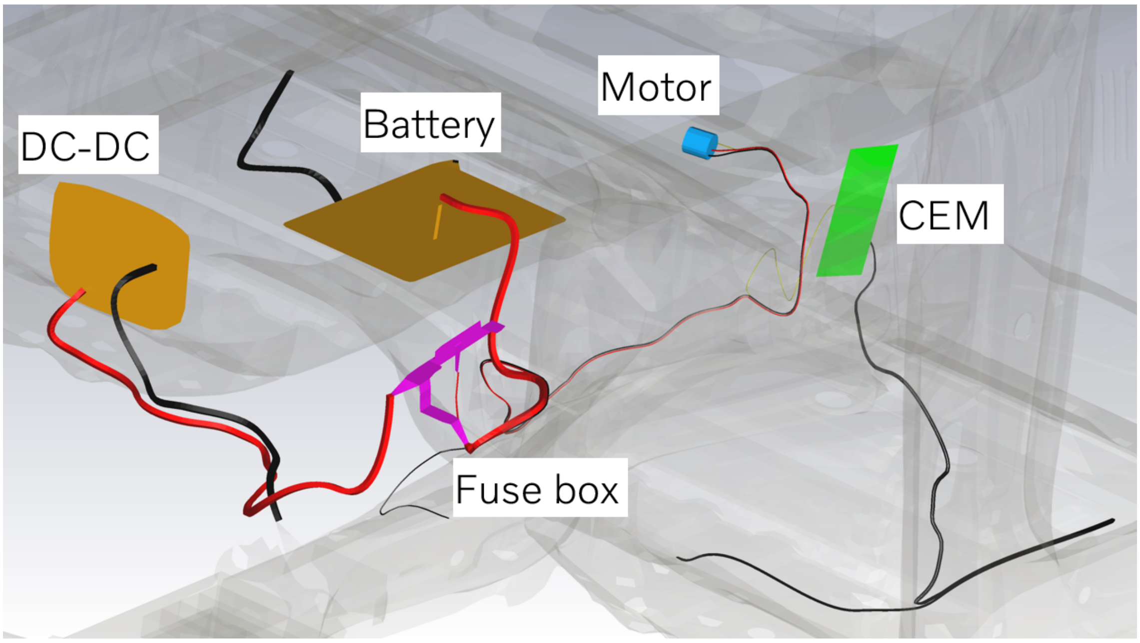

Figure 6.3: Zoomed 3D view highlighting the locations of the wiper motor, battery, DC–DC, fuse box, and CEM within the engine bay, together with nearby harness segments relevant to CM return closure.

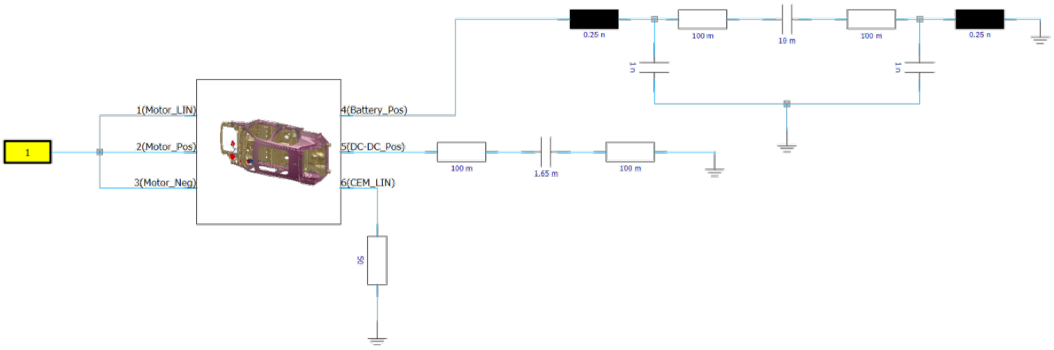

Figure 6.4: Schematic network with six ports. Ports 1–3 are the motor-side terminals driven by the CE-derived CM source. Port 4 connects to the internal equivalent circuit of the 12 V battery. Port 5 connects to the internal equivalent circuit of the DC–DC converter. Port 6 is the signal input terminated to 50 Ω to ground.

6.4 Observation Geometry and Readout

Two complementary readouts are employed.

6.4.1 ECE R10 External Readout

Following the ECE Regulation R10 vehicle-level layout, a biconical antenna is placed 3 m from the vehicle side at a height of 1.8 m. The induced voltage across a lumped element in the antenna model is converted to electric-field strength through the antenna factor (AF) using the additive rule in dB units identical to Eq. (5.1) in Section 5.4. In view of prior project experience that higher-frequency (>200 MHz) radiation is negligible for this DUT class, the external readout is evaluated over 30 MHz to 200 MHz. A 3D layout indicating the antenna entity and its placement is shown in Fig. 6.5.

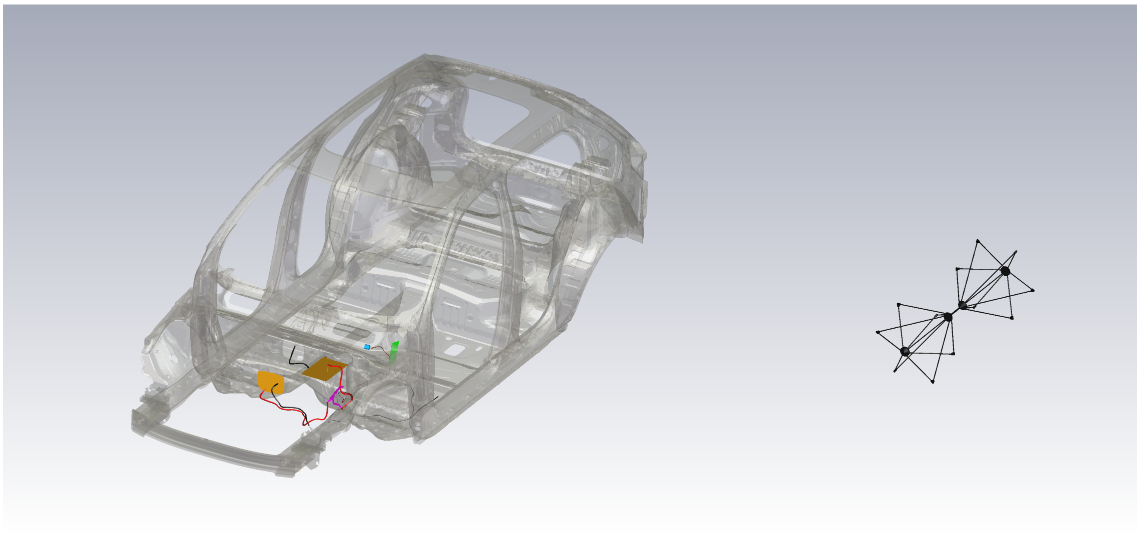

Figure 6.5: 3D layout of the ECE R10 external readout: biconical antenna entity positioned at 3 m from the vehicle side and 1.8 m height.

6.4.2 Engine-Bay Near Fields

Four electric-field probes are placed in close proximity to key modules; their coordinates are summarized in Table 6.1. The probe magnitude is reported in dB μV/m from 0.15 MHz to 320 MHz. Field monitors are additionally used to visualize surface-current distribution on the harness and to inspect field spreading with frequency.

Table 6.1: Coordinates of the four near-field E-field probes (mm).

Location	x	y	z
Fuse box	1500	−550	900
DC–DC	1500	0	800
Battery	1700	−350	900
Motor	2000	−550	1000

6.5 Solver Configuration and Reproducibility

All runs use the frequency-domain solver of *CST Studio Suite* version 2025.4 (released on 2025-04-11) on Linux. The solver reports two CPU devices and 32 threads. A sparse broadband sweep is evaluated between 0.15 MHz and 320 MHz. Representative anchor points include $\{320, 296.158, 274.092, \ldots, 1.03935, 0.961913\}$ MHz, and the reporting grid contains 77 calculation points. Any invalid user sampling entries are ignored while honoring the lower bound at 0.15 MHz.
The mesh is tetrahedral with variable second-order settings and curved elements up to third order (automatic). Adaptive mesh refinement proceeds through four passes: mesh cells increase from 805,396 to 1,012,907. The solver-reported S-parameter deltas decrease from 0.329052 (after pass 2) to 0.0221386 (pass 3) and 0.0182488 (pass 4), upon which the desired accuracy limit is reached and adaptation stops. The log records local curvature reduction and some low-quality tetrahedra but does not print numerical edge-ratio or quality statistics. Coefficient and mesh backups are disabled; solutions are not archived. The total simulation time is 2 h 20 min 30 s.

6.6 Results

6.6.1 ECE R10 External Readout (30–200 MHz)

Under the regulation layout (3 m distance, 1.8 m height), the predicted electric field is *very low* across 30 MHz to 200 MHz. Fig 6.6 illustrates the predicted spectrum under this ECE R10 external readout configuration, showing that it lies below the historical background levels observed in comparable laboratory campaigns and remains well below the applicable limits. *For small-power devices of this class, the contribution to vehicle-level far-field radiation is practically negligible for compliance purposes; therefore, the analysis shifts to whether the device's near-field radiation could interfere with other engine-bay electronics.*

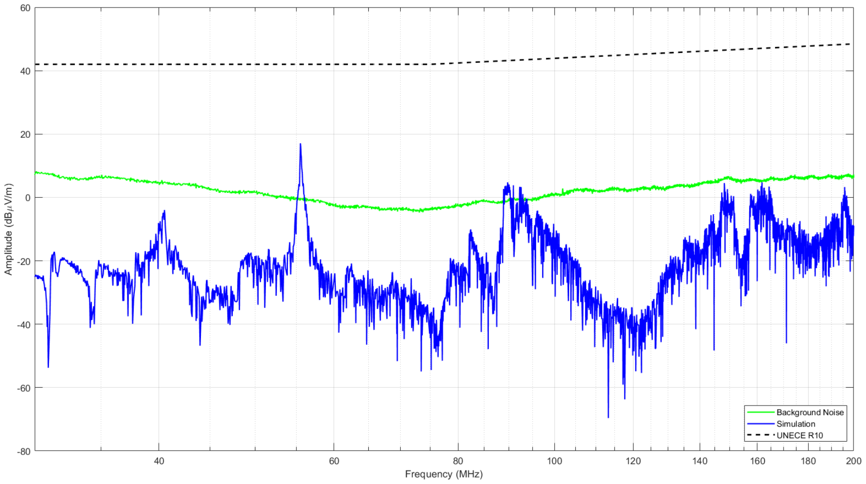

Figure 6.6: Predicted electric-field strength over 30 MHz to 200 MHz.

6.6.2 Engine-Bay Near-Field Probes (150 kHz–320 MHz)

The near-field overlay in Fig. 6.7 shows a pronounced spatial gradient in the low-frequency band. Between 0.15 MHz and 30 MHz, the probe adjacent to the motor exceeds the other three locations by approximately 40 dBµV/m to 80 dBµV/m across broad intervals. The battery, DC–DC, and fuse-box probes are mutually close in magnitude. *These results suggest a possibility of local interference risk in the immediate vicinity of the motor for sensitive co-located electronics; a dedicated susceptibility assessment would be the appropriate next step.*

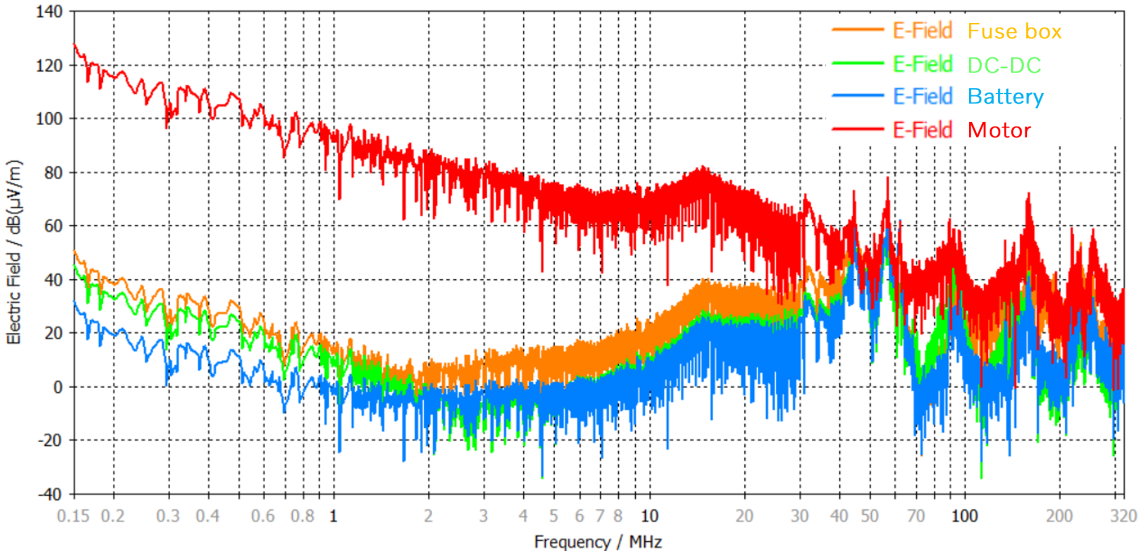

Figure 6.7: Near-field probe overlay at the four engine-bay locations from 0.15 MHz to 320 MHz. Probe coordinates are listed in Table 6.1.

6.6.3 Surface-Current Distributions by Supply Mode

To visualize current partitioning under different operating conditions, surface-current density is post-processed on the BIW and harness for the three supply modes. Fig 6.8 compares the distributions for the battery-only, DC–DC-only, and dual-supply configurations: the harnesses participating in the active supply path carry stronger currents, and the return closure follows the available contacts to the BIW. These patterns support the near-field observations and indicate where local mitigation would be most effective.

6.6.4 Frequency Evolution of Field Distributions

Representative snapshots at four frequencies illustrate the low-frequency concentration near the motor and the increasing spatial spread along the harness with frequency. *As frequency increases, absolute levels decrease, yet the field spreads farther along the harness network, so enhanced fields emerge on segments located farther from the motor.* Fig 6.9 assembles the {0.15, 15, 73, 320} MHz distributions in a 2×2 layout for side-by-side comparison.

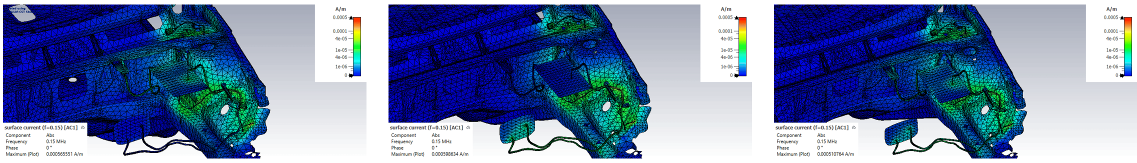

(a) Battery-only **(b)** DC–DC-only **(c)** Dual supply

Figure 6.8: Surface-current distributions for the three supply modes. Stronger currents align with the active supply branch and its immediate BIW return paths, consistent with near-field enhancements observed around corresponding harness segments.

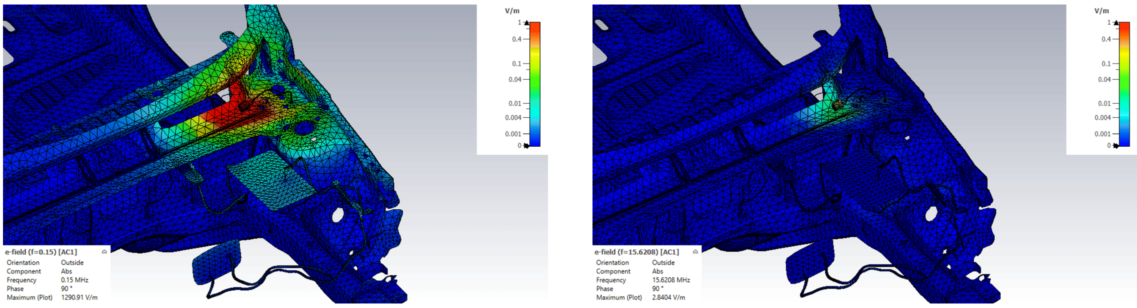

(a) 0.15 MHz **(b)** 15 MHz

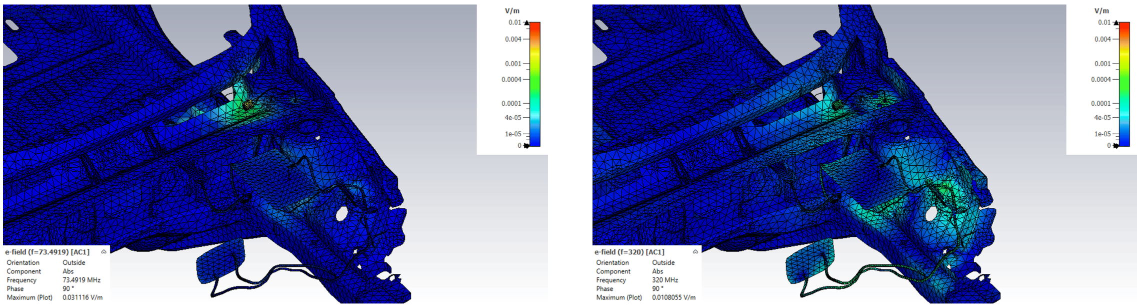

(c) 73 MHz **(d)** 320 MHz

Figure 6.9: Field-distribution snapshots at four frequencies. Low-frequency fields peak near the motor; with increasing frequency the absolute level decreases while spatial spreading along the harness increases.

6.7 Limits of Validity

All conductive structures other than harness conductors are modeled as PECs. Modeling all non-harness conductors as PECs overestimates the structural shielding and enforces low-impedance return paths on the BIW, which tends to reduce the predicted radiation levels and is conservative with respect to radiated-emission risk. No vehicle-level measurements were conducted in this project. Accordingly, the predictions are suited to diagnosing mechanisms, spatial trends, and the ordering of levels across locations and operating modes; they are not a substitute for regulatory compliance testing per ECE R10.

6.8 Chapter Summary

A full-vehicle EM model with CE-derived excitation was used to predict E-fields from 0.15 MHz to 320 MHz. Under the ECE R10 external layout (3 m, 1.8 m), predicted fields over 30 MHz to 200 MHz are very low; for small-power devices of this class, the far-field contribution is negligible for compliance purposes, so attention shifts to the engine bay. Near-field analysis shows that the motor-adjacent location exceeds other points by 40 dBµV/m to 80 dBµV/m in 0.15 MHz to 30 MHz. Frequency snapshots further show that absolute levels fall with frequency while the field spreads farther along harness routes. Surface-current maps across the three supply modes corroborate these findings and highlight the segments where local mitigation would be most effective.

7

Conclusion

This thesis has addressed the challenge of predicting vehicle-level electromagnetic compatibility (EMC) performance from component-level testing and modeling, with a focus on the automotive wiper drive system as a representative case study. The research was motivated by the need to reduce reliance on costly and time-consuming late-stage vehicle-level testing and to establish methodologies that enable earlier identification and mitigation of EMC problems. By combining experimental measurements conducted according to CISPR 25 with advanced numerical simulations using CST Studio Suite, this study demonstrated both the feasibility and the challenges of using component-level data as the foundation for whole-vehicle EMC prediction.

At the component level, a dedicated load fixture was designed, and EMC tests of the wiper motor were conducted in a semi-anechoic chamber. The measured data showed good consistency with supplier-provided results, validating the reliability of the experimental setup. In addition to verifying compliance, these measurements provided valuable input parameters for simulation-based analysis. The comparison of simulated and measured electric fields across the frequency range of 150 kHz–30 MHz demonstrated close agreement, confirming that radiated emissions can be reliably predicted when measured conducted current is used as the excitation source in the simulation model. This approach establishes a practical framework for integrating empirical data with numerical simulation, significantly enhancing the predictive accuracy of component-level analyses.

The component-level simulation work highlighted the value of combining measurement-based parameters with high-fidelity electromagnetic modeling. The results indicate that radiated disturbances can be effectively captured by appropriately defined source models, and that iterative refinement of simulation parameters such as material properties, boundary conditions, and grounding strategies further improves predictive accuracy. Importantly, this work illustrates that reliable component-level models provide the foundation for system-level analysis, bridging the gap between bench tests and full-vehicle evaluations.

At the vehicle level, preliminary simulations were developed to extend the scope of the component-based approach. Unlike conventional standard-based far-field analysis, this work emphasized near-field simulation in order to better represent the local coupling mechanisms between components, wiring harnesses, and the vehicle body. Models were built and executed under multiple scenarios, exploring the influence of installation configurations and grounding strategies. While the initial results are promising, full validation against experimental vehicle-level data is still pending and remains an important task for future work. Nonetheless, the methodological framework established here provides a pathway for scaling up from component models to system-level prediction.

The outcomes of this research lead to several important conclusions. First, the study demonstrates that component-level simulation and testing, when carefully integrated, can reproduce key aspects of vehicle-level EMC performance. This capability provides engineers with a tool to identify potential EMC hazards earlier in the development cycle, reducing the number of costly redesigns and repeated prototype tests. Second, the findings highlight the practical challenges of this approach. Accurate characterization of interference sources, particularly in components such as brushed DC motors with transient broadband emissions, remains a significant difficulty. Similarly, representing the full electromagnetic environment of a vehicle—including body structures, wiring harnesses, and interactions among multiple subsystems—poses substantial modeling and computational challenges. These limitations underscore that simulation, in its current state, cannot fully replace physical vehicle-level testing.

Nevertheless, the engineering significance of this work is considerable. By demonstrating that component-level models can reliably reproduce measured behavior and be scaled toward vehicle-level prediction, this study provides a foundation for a hybrid development methodology in which simulation and testing complement each other. In practical terms, simulations can be used to narrow down potential problem areas, optimize design elements such as filtering, shielding, and grounding, and guide system integration. Physical vehicle tests can then serve as targeted validation steps rather than broad diagnostic exercises. This combined approach has the potential to reduce development time, lower costs, and enhance design robustness, aligning with industry goals for faster and more efficient product development.

Looking forward, several future research directions emerge from this study. Advances in high-performance computing (HPC) will enable more detailed and computationally intensive models, including the integration of full-vehicle structures and long wiring harnesses without oversimplification. The incorporation of artificial intelligence and machine learning holds promise for accelerating model development, automating parameter tuning, and guiding design optimization across multi-dimensional trade-offs such as cost, weight, and EMC performance. Furthermore, the emergence of digital twin technologies offers the possibility of real-time EMC prediction and monitoring, with virtual models continuously updated by experimental and operational data. This evolution may eventually lead to simulation-based compliance assessments, reducing reliance on conventional testing frameworks.

In conclusion, this thesis has demonstrated that component-level EMC testing and simulation provide a reliable and practical basis for predicting vehicle-level performance, while also revealing the limitations that must be addressed for broader industrial adoption. Although simulation cannot yet fully replace experimental validation, it is an increasingly powerful complement to traditional testing. As simulation methodologies mature and gain industry recognition, their role in the EMC development process will continue to expand. For OEMs and component suppliers, the ability to effectively implement these tools will become a critical competency for ensuring compliance with evolving standards and maintaining competitiveness in the era of electrification, connectivity, and intelligent automotive systems.

8

Future Work

8.1 Background

The present work demonstrates the feasibility of predicting vehicle-level EMC tendencies based on component-level measurements and simulation. Although the proposed workflow provides a practical foundation, several extensions remain necessary to establish a more comprehensive and production-ready methodology.

8.1.1 Continuation of the Project and Full Vehicle Testing

The most direct next step is to complete the physical vehicle-level EMC tests for the same wiper motor system. These measurements will provide empirical correlation with the simulation-based predictions and allow detailed evaluation of discrepancies near-field probe distributions and BIW-induced resonances. Such validation is essential for refining or recalibrating the full-vehicle model.

8.1.2 Extension of the Modelling Framework to Additional Vehicle Structures and Subsystems

The current vehicle-level model applies simplified BIW geometry and idealized material definitions. Future work should incorporate additional components that significantly influence electromagnetic behaviour, such as fenders, brackets, cable routing hardware, shielding structures, and detailed grounding networks.
Furthermore, extending the methodology beyond the wiper motor to other noise-critical subsystems—for example HVAC blowers, window actuators, low-voltage pumps, and communication interfaces such as LIN, CAN, and Automotive Ethernet—would provide a broader validation basis for the component-to-vehicle prediction concept. This expansion would also support the development of a unified modelling framework for diverse automotive EMC sources.

8.1.3 Improved Source Modelling for Commutation-Based Emissions

The broadband noise generated by brushed motors is strongly dependent on commutation dynamics. Future work should include enhanced electrical and mechanical representations of the commutator, brush geometry, and load torque. Hybrid time-domain circuit–field co-simulation may substantially improve the accuracy of the

CE-derived excitation used in full-wave modelling.

8.1.4 Integration into Simulation-Supported EMC Development Workflow

In the long term, the goal is to incorporate validated models into a simulation-supported EMC development process, where component-level virtual assessments can be used to pre-screen designs before vehicle integration. This approach would reduce the number of physical prototypes and shorten the development cycle, supporting more efficient EMC compliance throughout the design stage.

Bibliography

[1] C. Christopoulos, *Principles and techniques of electromagnetic compatibility.* CRC press, 2022.

[2] M. E. Abdurrahim, “Analysis and evaluation of uncertainty for conducted and radiated emissions tests,” Ph.D. dissertation, Universiti Tun Hussein Malaysia, 2013.

[3] L. Jiang, H. Liu, and C. Wang, “Summary of emc test standards for wireless power transfer systems of electric vehicles,” in *2021 Asia-Pacific International Symposium on Electromagnetic Compatibility (APEMC).* IEEE, 2021, pp. 1–4.

[4] B. Wang, S. Zhang, and Z. Zhang, “A model-based approach to evaluate electromagnetic responses in vehicle control systems influenced by harness shielding and grounding,” in *2024 IEEE International Conference on Advanced Information, Mechanical Engineering, Robotics and Automation (AIMERA).* IEEE, 2024, pp. 261–268.

[5] L. A. Kumar and Y. U. Maheswari, *Electromagnetic interference and electromagnetic compatibility: principles, design, simulation, and applications.* CRC Press, 2023.

[6] M. I. Montrose, *EMC and the printed circuit board: design, theory, and layout made simple.* John Wiley & Sons, 2004.

[7] P. Andersen, “The present status of the international automotive emc standards,” in *2009 IEEE International Symposium on Electromagnetic Compatibility.* IEEE, 2009, pp. 98–102.

[8] ——, “An overview of automotive emc standards,” in *2006 IEEE International Symposium on Electromagnetic Compatibility, 2006. EMC 2006.*, vol. 3. IEEE, 2006, pp. 812–816.

[9] K. Arslan, S. Kiyak, and E. E. Atalay, “Examination of the different measurement angles on radiated emission tests of electronic and electrical components according to cispr 25,” in *2023 7th International Electromagnetic Compatibility Conference (EMC Turkiye).* IEEE, 2023, pp. 1–5.

[10] J. Jia, D. Rinas, and S. Frei, “Predicting the radiated emissions of automotive systems according to cispr 25 using current scan methods,” *IEEE Transactions on Electromagnetic Compatibility*, vol. 58, no. 2, pp. 409–418, 2016.

[11] A. Hofer and S. Cecil, “Numerical simulation of field distribution regarding automotive component emc-testing according to iso 11452–2,” in *2022 International Symposium on Electromagnetic Compatibility–EMC Europe.* IEEE, 2022, pp. 399–404.

[12] V. Rodriguez, “Automotive component emc testing: Cispr 25, iso 11452–2 and equivalent standards,” *IEEE electromagnetic compatibility magazine*, vol. 1, no. 1, pp. 83–90, 2012.

[13] A. R. Ruddle and A. J. Martin, “Adapting automotive emc to meet the needs of the 21st century,” *IEEE Electromagnetic Compatibility Magazine*, vol. 8, no. 3, pp. 75–85, 2019.

[14] R. K. Frazier and S. Alles, “Comparison of iso 7637 transient waveforms to real world automotive transient phenomena,” in *2005 International Symposium on Electromagnetic Compatibility, 2005. EMC 2005.*, vol. 3. IEEE, 2005, pp. 949–954.

[15] J. Hein, J. Hippeli, and T. F. Eibert, “Efficient emc parameter analysis for the verification of complex automotive simulation models by the utilization of design of experiments,” *IEEE Transactions on Electromagnetic Compatibility*, vol. 60, no. 6, pp. 1965–1973, 2018.

[16] C. Wu, F. Gao, H. Dai, and Z. Wang, “A topology-based approach to improve vehicle-level electromagnetic radiation,” *Electronics*, vol. 8, no. 3, p. 364, 2019.

[17] F. Gao, H. Dai, J. Qi, and Z. Wang, “Vehicle-level electromagnetic compatibility prediction based on multi-port network theory,” *International Journal of Automotive Technology*, vol. 20, no. 6, pp. 1277–1285, 2019.

[18] I. Hänninen, F. Wolfheimer, A. Barchanski, and D. Kostka, “High performance computing techniques for efficient 3d full-wave simulation of emc problems,” in *2014 International Symposium on Electromagnetic Compatibility, Tokyo.* IEEE, 2014, pp. 828–831.

[19] C. Bleoju, A.-M. Silaghi, and A. De Sabata, “Simulation and measurement of conducted emissions–current probe in automotive emc,” in *2021 International Symposium on Signals, Circuits and Systems (ISSCS).* IEEE, 2021, pp. 1–4.

[20] L. B. Wang, L. Ma, and E. A. Koh, “Analyzing the emc performance of an automotive display module through 3d electromagnetic simulation,” in *2018 IEEE International Symposium on Electromagnetic Compatibility and 2018 IEEE Asia-Pacific Symposium on Electromagnetic Compatibility (EMC/APEMC).* IEEE, 2018, pp. 827–830.

[21] R. G. Jobava, A. L. Gheonjian, J. Hippeli, G. Chiqovani, D. D. Karkashadze, F. G. Bogdanov, B. Khvitia, and A. G. Bzhalava, “Simulation of low-frequency magnetic fields in automotive emc problems,” *IEEE Transactions on Electromagnetic Compatibility*, vol. 56, no. 6, pp. 1420–1430, 2014.

[22] S. Güler, S. Yenikaya, and M. Şimşek, “Emc design for battery electric vehicle (bev) propulsion system,” in *2019 11th International Conference on Electrical and Electronics Engineering (ELECO).* Ieee, 2019, pp. 286–289.

[23] R. Murugan, J. Chen, A. Tripathi, B. P. Nayak, H. Muniganti, and D. Gope, “Multiscale emc modeling, simulation, and validation of a synchronous step-down dc-dc converter,” *IEEE Journal on Multiscale and Multiphysics Computational Techniques*, vol. 8, pp. 269–280, 2023.

[24] S. Ahmed, “Hfss enables the simulation of electromagnetic pulses and predicts its effects,” in *2023 IEEE Symposium on Electromagnetic Compatibility & Signal/Power Integrity (EMC+ SIPI).* IEEE, 2023, pp. 473–473.

[25] Q. Ming, Y. Wang, and M. Zong, "Research on emc simulation of electric drive system of electric engineering machinery," in *International Conference on Advances in Construction Machinery and Vehicle Engineering.* Springer, 2023, pp. 231–246.

[26] A.-M. Silaghi and A. De Sabata, "Analysis of radiated immunity of an automotive display by means of testing and simulation," in *2020 43rd International Conference on Telecommunications and Signal Processing (TSP).* IEEE, 2020, pp. 73–76.

[27] A. Tsukioka, M. Nagata, K. Taniguchi, D. Fujimoto, R. Akimoto, T. Egami, K. Niinomi, T. Yuhara, S. Hayashi, R. Mathews *et al.*, "Simulation techniques for emc compliant design of automotive ic chips and modules," in *2017 International Symposium on Electromagnetic Compatibility-EMC EUROPE.* IEEE, 2017, pp. 1–6.

[28] S. Pan, P. Jiang, and B. Bao, "Equivalent realisation circuit for a class of nonideal voltage-controlled memristors," *The Journal of Engineering*, vol. 2015, no. 12, pp. 354–356, 2015.

[29] N. Idir, Y. Weens, M. Moreau, and J.-J. Franchaud, "High-frequency behavior models of ac motors," *IEEE Transactions on Magnetics*, vol. 45, no. 1, pp. 133–138, 2009.

[30] J. F. Mologni, M. Kopp, A. Colin, M. A. Alves, and E. S. Braga, "Full vehicle electromagnetic simulation using the hybrid finite element boundary integral approach," SAE Technical Paper, Tech. Rep., 2011.

[31] E. Panholzer, M. Spägele, H. Leier, and S. Lindenmeier, "In-car emission prediction for a real communication system based on a component level test," in *2018 International Symposium on Electromagnetic Compatibility (EMC EUROPE).* IEEE, 2018, pp. 72–77.

[32] J. F. Dos Santos, B. K. Tshoombe, L. H. Santos, R. C. Araújo, A. R. Manito, W. S. Fonseca, and M. O. Silva, "Digital twin-based monitoring system of induction motors using iot sensors and thermo-magnetic finite element analysis," *IEEE access*, vol. 11, pp. 1682–1693, 2022.

[33] D. M. Ninković and D. I. Olćan, "Ai-assisted identification of state and type of flat-panel monitors in the presence of em noise," *IEEE Transactions on Electromagnetic Compatibility*, vol. 66, no. 4, pp. 1057–1067, 2024.

[34] F. Robert, M. Bensetti, F. V. dos Santos, L. Dufour, and P. Dessante, "Multiphysics modeling and optimization of a compact actuation system," *IEEE Transactions on Industrial Electronics*, vol. 64, no. 11, pp. 8626–8634, 2017.

A

Appendix

A.1 VAMP 9243 (100 kHz–30 MHz)

This section provides the antenna factor (AF) as a function of frequency for the VAMP 9243 monopole in the band 100 kHz–30 MHz. Detailed frequency points are provided in the accompanying CSV.

Table A.1: Summary statistics of the antenna factor for VAMP 9243 (100 kHz–30 MHz).

Metric	Value	Note
Frequency span	0.1–30.0 MHz	7476 points
$\mathrm{AF}_{\mathrm{min}}$	10.12 dB/m	within band
$\mathrm{AF}_{\mathrm{median}}$	10.26997 dB/m	—
$\mathrm{AF}_{\mathrm{max}}$	10.38804 dB/m	within band

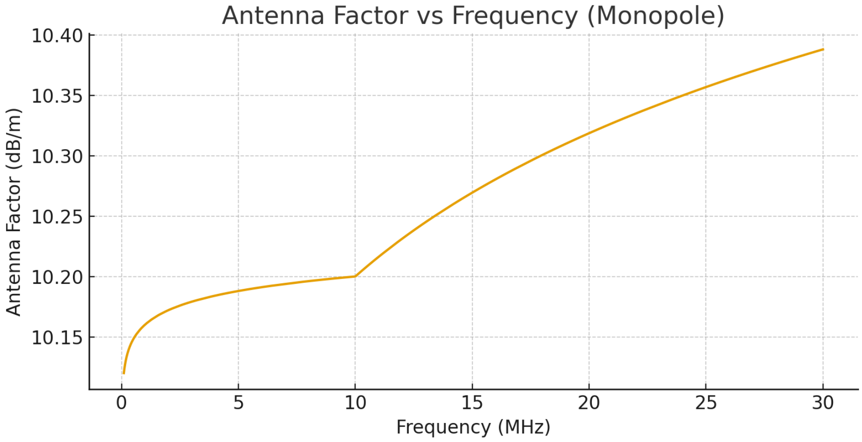

Figure A.1: Antenna factor versus frequency for the VAMP 9243 monopole (100 kHz–30 MHz).

A.2 BBVK 9138 + VHA 9103 (30–200 MHz)

This section provides the antenna factor (AF) as a function of frequency for the BBVK 9138 biconical assembly mounted in the VHA 9103 balun/holder over 30–

200 MHz. Detailed frequency points are provided in the accompanying CSV.

Table A.2: Summary statistics of the antenna factor for BBVK 9138 + VHA 9103 (30–200 MHz).

Metric	Value	Note
Frequency span	30.0–200.0 MHz	4251 points
$\mathrm{AF}_{\mathrm{min}}$	10.75642 dB/m	within band
$\mathrm{AF}_{\mathrm{median}}$	18.23895 dB/m	—
$\mathrm{AF}_{\mathrm{max}}$	21.96322 dB/m	within band

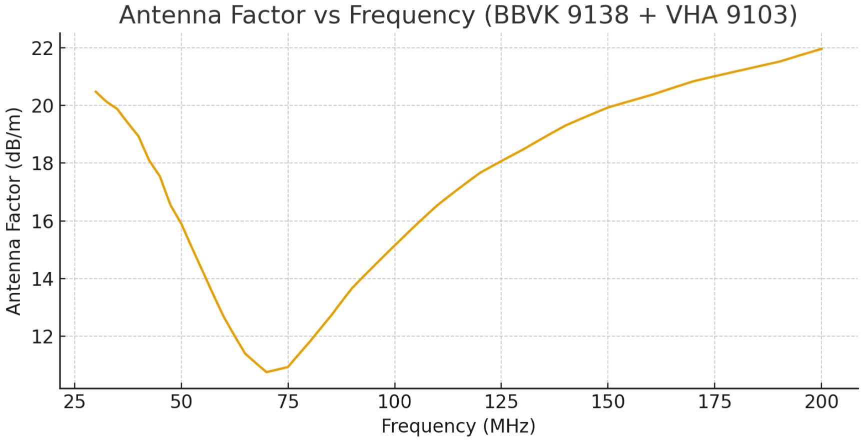

Figure A.2: Antenna factor versus frequency for BBVK 9138 + VHA 9103 (30–200 MHz).

A.3 ETS-Lindgren 3147 (200–1000 MHz)

This section provides the antenna factor (AF) as a function of frequency for the ETS-Lindgren 3147 log-periodic dipole array (LPDA) over 200–1000 MHz. Detailed frequency points are provided in the accompanying CSV.

Table A.3: Summary statistics of the antenna factor for ETS-Lindgren 3147 (200–1000 MHz).

Metric	Value	Note
Frequency span	200.0–999.96 MHz	20000 points
$\mathrm{AF}_{\mathrm{min}}$	15.77322 dB/m	within band
$\mathrm{AF}_{\mathrm{median}}$	23.07368 dB/m	—
$\mathrm{AF}_{\mathrm{max}}$	27.86695 dB/m	within band

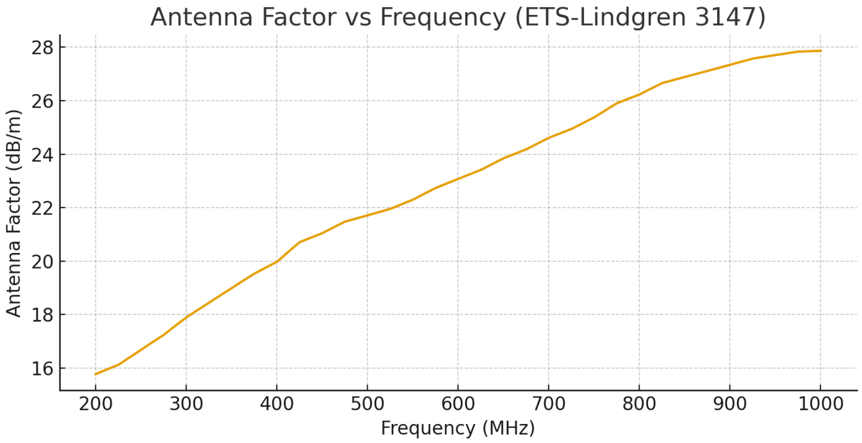

Figure A.3: Antenna factor versus frequency for ETS-Lindgren 3147 (200–1000 MHz).

A.4 R&S HFH2-Z2E (150 kHz–30 MHz)

This section provides the antenna factor (AF) as a function of frequency for the R&S HFH2-Z2E loop over 150 kHz–30 MHz. Detailed frequency points are provided in the accompanying CSV.

Table A.4: Summary statistics of the antenna factor for R&S HFH2-Z2E (150 kHz–30 MHz).

Metric	Value	Note
Frequency span	0.15–30.0 MHz	7464 points
AF_{min}	-31.33054 dB/m	within band
AF_{median}	-31.28162 dB/m	—
AF_{max}	-30.94196 dB/m	within band

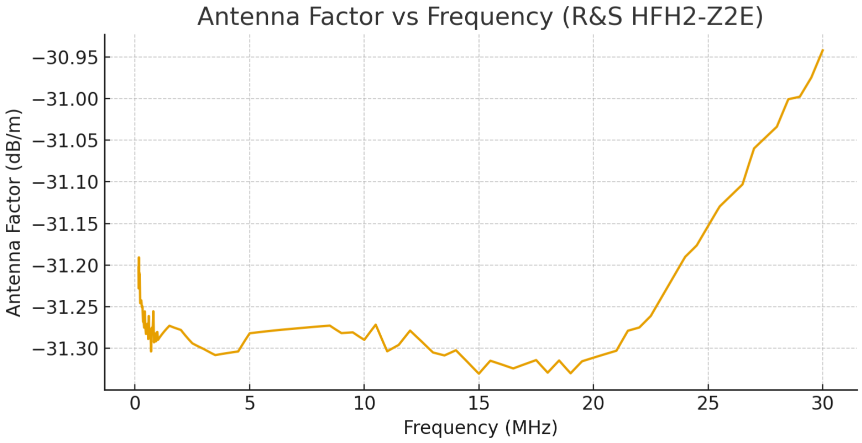

Figure A.4: Antenna factor versus frequency for R&S HFH2-Z2E (150 kHz–30 MHz).

DEPARTMENT OF SOME SUBJECT OR TECHNOLOGY
CHALMERS UNIVERSITY OF TECHNOLOGY
Gothenburg, Sweden
www.chalmers.se